CFD SIMULATION OF THE INFLUENCE OF VISCOSITY ON AN ELECTRICAL SUBMERSIBLE PUMP

A Thesis

by

WENJIE YIN

Submitted to the Office of Graduate and Professional Studies of
Texas A&M University
in partial fulfillment of the requirements for the degree of

MASTER OF SCIENCE

Chair of Committee,	Gerald L. Morrison
Committee Members,	Michael B. Pate
	Karen Vierow
Head of Department,	Andreas A. Polycarpou

August 2016

Major Subject: Mechanical Engineering

ABSTRACT

Electrical Submersible Pump (ESP) is a multi-stage centrifugal pump used in the petroleum industry. Due to the high efficiency and adaptivity, ESPs are widely employed in offshore oil wells. Viscous fluid pumping can result in degradation of ESP performance. Improving the efficiency and maintaining the performance of ESPs are of great significance to oil production economic benefit.

To better understand the influence of viscosity on electrical submersible pumps, this work uses a CFD method to study the flow behaviors inside ESPs. Commercial software ANSYS Fluent is adopted to simulate the flow field inside the pump. A single stage of an ESP WJE-1000, manufactured by Baker Hughes Ltd., is modelled and investigated. 3-D single phase flow numerical simulation is performed to study the pump performance. Several sets of fluids of different viscosities and densities are tested under various operation conditions. A wide range of inlet flow rates are calculated for every set of fluids.

The effects of viscosity on ESP performance is identified and studied thoroughly. The flow field inside the pump channels is explored by post processing software. To understand how pump performance changes under different testing conditions, dimensionless analysis is performed. Shaft power, hydraulic power and drag power are discussed and calculated by dimensionless numbers.

DEDICATION

To my parents and my lovely Kaimi

ACKNOWLEDGEMENTS

I would like to express my sincere appreciation and thanks to Dr. Gerald Morrison for his guidance and support on my work. His knowledge, intelligence and patience helped me to solve various problems throughout the research.

Also, I would like to thank my committee members, Dr. Michael Pate and Dr. Karen Vierow for their selfless support.

Thanks to Yiming Chen, Abhay Patil and Sujan Reddy for their unconditionally help on my work.

Thanks also go to all my colleagues at TurboLab, Yi Chen, Changrui Bai, Yintao Wang, Wenfei Zhang, Peng Liu, Ke Li and Bahadir Basaran, for making my time at Texas A&M University a great experience.

Finally, thanks to my father and mother for their encouragement and patience throughout my research.

NOMENCLATURE

ESP	Electrical Submersible Pump
GVF	Gas Volume Fraction
BEP	Best Efficiency Point
RMS	Root Mean Square
D	Diameter
D_h	Hydraulic diameter
A_{in}	Inlet cross section area
D_s	Length scale of the pump geometries
Q	Volumetric flow rate
P	Pressure
ΔP	Pressure difference
H	Head
T	Torque
P_{sh}	Shaft power
P_{drag}	Drag power
N_{sh}	Shaft power coefficient
N_{out}	Output power coefficient
N_{drag}	Drag power coefficient
Re_{Dh}	Reynolds number based on the hydraulic diameter
Re_w	Rotating Reynolds number
g	Gravitational acceleration
gpm	Gallons per minute
rpm	Revolutions per minute
h	Blade height
t	Blade thickness

Greek Letters

ρ	Density of the testing fluid
μ	Dynamics viscosity
v	Kinematic viscosity
ω	Angular speed
η	Pump efficiency
Φ	Flow rate coefficient
Ψ	Head coefficient

Subscripts

w	Value in water cases
v	Value in oil cases
1	Impeller inlet
2	Impeller outlet
3	Diffuser inlet
4	Diffuser outlet
i	Inner circle
o	Outer circle

TABLE OF CONTENTS

Page

LIST OF FIGURES

Page

LIST OF TABLES

Page

I. INTRODUCTION

In the oil field development process, due to the formation energy depleting, the decreasing pressure head does not allow the reservoir to keep flowing through the wells. Some reservoirs are originally low in pressure for natural flow. When the production rate is not satisfactory, artificial lift methods have to be applied.

The commonly used artificial lift methods in the oil and gas industries are shown in Figure I-1. From left to right are rod pumps, progressing cavity pumps, horizontal surface pumps, electrical submersible pumps and gas lift. The selection of method depends on economic, environmental and applicable requirements for different oil wells.

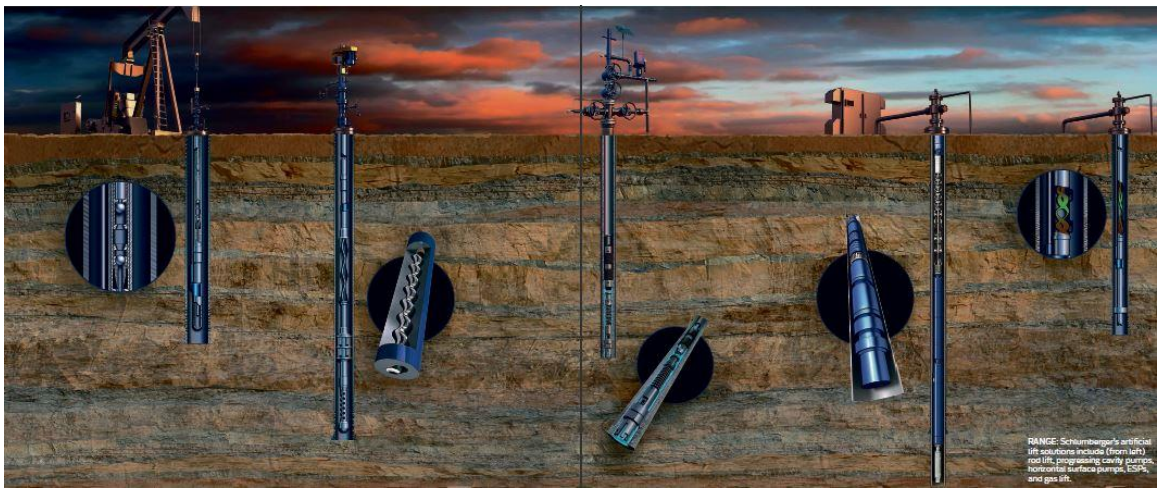

Figure I-1: Artificial lift methods illustration [1]

The rod pump is the most classic artificial lift method in the oil industry. A rod pump system normally consists of a pump jack, a sucker rod pump and a sucker rod

string. The sucker rod string transfers movement and energy from the pump jack on the ground to the underground sucker rod pump. The sucker rod pump lifts the fluids to the surface by putting high pressure on the fluids. The equipment for a rod pump system is inexpensive and reliable, which makes this method the mostly widely used and the most mature technology among artificial lift methods. The limit of a rod pump system is its poor performance in lifting high viscous fluids. Progressing cavity pumps have a long history. Inside a progressing cavity pump, fluids are pushed upwards by the screw blades. The fluids are lifted by one thread pitch in every rotation cycle. Progressing cavity pumps have good performance in pumping high viscosity fluids. The disadvantage of this type of pump is the high maintenance cost as the screws are vulnerable. Horizontal surface pumps are one type of arrangements of centrifugal pumps. The horizontal arrangement of surface units is beneficial for installing equipment and maintenance. Thus horizontal arrangement is often the first choice for economic requirement. The disadvantage of a horizontal surface pump is its weak applicability under different working conditions, which leads to limited usage in the offshore oil wells. Gas lift is a promising artificial lift method in both the downhole and the offshore petroleum industries. In the gas lift method, high pressure gas (CH4, N2, or CO2) is injected into the oil wells. The mixture of oil and injected gas has lower density and higher pressure. Then enough energy is provided for the mixed fluids to flow through the wells. Gas lift method is versatile and well performed under different geometrical conditions. So despite of the high initial investment, gas lift is used in a large amount of oil wells.

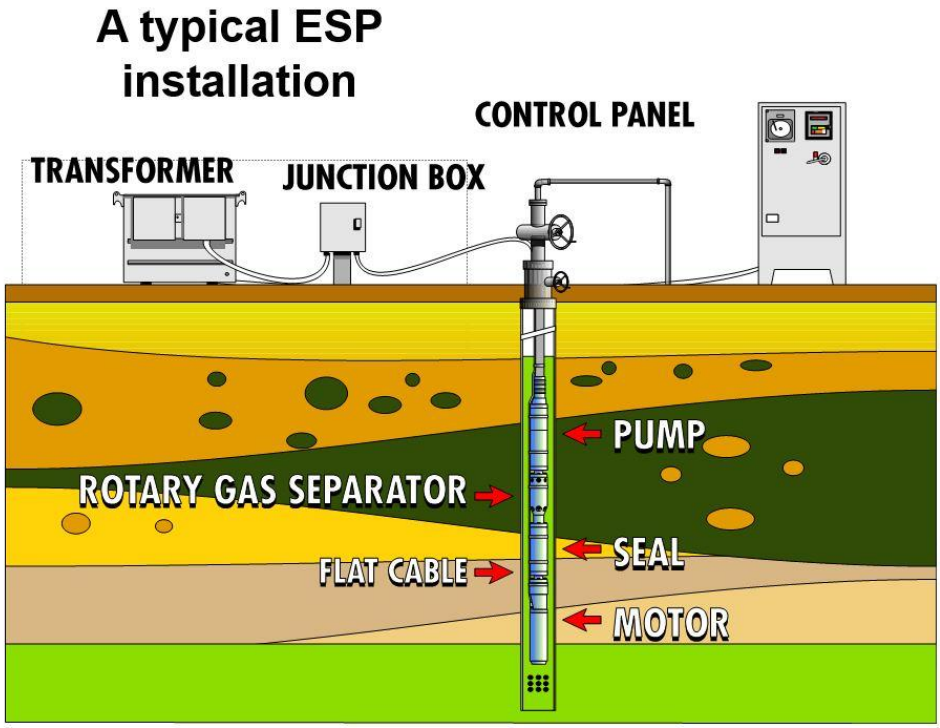

Figure I-2: Schematic view of the ESP system [2]

Electrical submersible pumps are the most commonly employed artificial lift method in offshore wells. Figure I-2 shows the schematic view of an entire ESP system. An ESP system consists of subsurface units and surface units. On the ground, there is a controller, a transformer and a junction box. Located in the well are an electric motor, a gas separator, a protector and a multistage pump, all work together to lift the oil from the bottom of the well.

During the lifting procedure, the transformer outputs the required working voltage from external inlet electricity. The control panel is the central control unit of the whole system. It provides the underground motor with electric power via flat cables through the well. When the motor is working, the pump is rotated along with the gas

separator. A protector is set around the motor. The protector seals the underground motor and balances the pressure between the motor and outside environment. The vital part of the whole system is the subsurface multistage pump. As the fluids enter the pump, they acquire pressure rise mainly from the impellers inside the pump. After a certain number of stages, the fluid has enough pressure to flow to the surface. Since the gas in the mixed fluids will degrade the head of the pump, a gas separator is usually located below the pump to lower the gas volume fraction (GVF) of the fluids.

The downhole pump is a multistage centrifugal pump. A view of the inner parts is shown in Figure I-3. As a centrifugal pump, the ESP has impellers and diffusers. The number of vanes of the impellers and diffusers varies according to the manufacture design. Commonly, there are five to seven blades in the impeller and similar number of vanes in the diffuser. A shaft is located in the axial position to transfer movement from the motor to the rotary parts. At the intake end, bolts are designed for seal. In most ESPs, the diffusers are stationary; the impellers are rotating along the shaft. When the impeller rotates about the axis of the pump, the fluids inside the stage are moved outward from the axis by centrifugal force. With the gained speed and pressure, the fluids flow along the flow paths and enter the stationary diffuser. The diffuser does not add energy to the working fluids. It transfers the speed of the fluids into pressure and leads the flow into next stage while trying to minimize energy loss. As the fluids flow through all impellers and diffuses, it obtains hydraulic head stage by stage. Eventually, the fluids have enough pressure to lift itself to the surface.

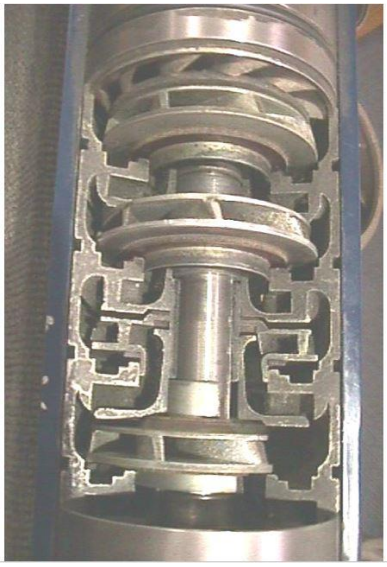

Figure I-3: Inner view of the ESP parts [2]

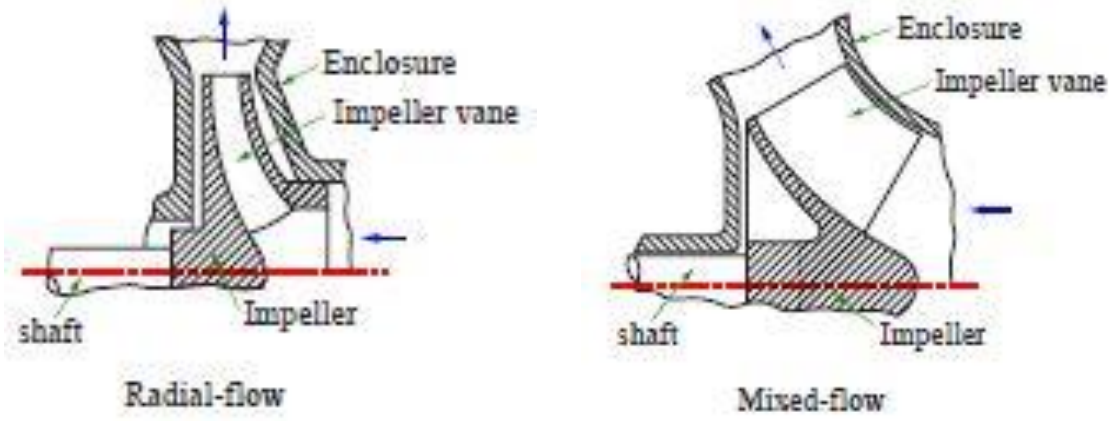

(a) (b)

Figure I-4: Comparison of radial-flow impeller and mixed-flow impeller [3]

Classified by the impeller design, there are two types of ESP pumps: radial-flow pumps and mixed-flow pumps. In a radial flow pump, as shown in Figure I-4(a), the fluids flow into the impeller axially and leave the impeller radially. The pressure rise in

this type of impeller is solely contributed by centrifugal force. Although the radial-flow pump has high hydraulic head, the restriction on flow rate limits its performance and usage. In a mixed-flow pump, as shown in Figure I-4(b), the fluids leave the impeller in an angle between axially and radially. The fluids are pushed away by centrifugal force and impeller shape. The design flow rate of mixed-flow pumps is commonly higher than radial-flow pumps.

Even considered as a reliable worldwide off shore petroleum production technology, ESPs have problems facing the complexity of oil fields. Multiphase flow, a mixture of fluids including gases, will lead to performance degradation. For high gas volume fraction fluids, free gas gathers at the suction, which lowers the pump efficiency. The gas may form gas lock which can stop fluid flow under certain conditions. Even in the simplest single phase flow cases, pumping highly viscous fluids can cause head degradation. Since the offshore oil field investment is extremely expensive, it is of great significance to perform researches on the performance of ESPs.

II. LITERATURE REVIEW

Karassik [4] introduced the fundamental concepts of centrifugal pumps. The detail structure of centrifugal pumps was shown and discussed. Performance characteristics of different types of pumps were comprehensively searched. The head curve of centrifugal pumps was analyzed to study the performance of centrifugal pumps.

Based on experiments, Ippen [5] used a specified Reynolds number R_D to study centrifugal pump performance. The kinematic viscosity of testing fluid was treated as one of the determinants of the Reynolds number. Corrections were introduced on head, power inlet and efficiency. It was concluded that all these parameters could be presented as a function of the Reynolds number $R_{D.}$ For Reynolds number less than 10^4 or more than 10^6, head correctors tend to be stable. In the analysis, when the Reynolds number is within the range of 10^4 to 10^6, disk and friction loss is thought to be the main reason for increasing power input. However, the result of the research is not applicable to other pumps.

Gulich [6], [7] gave a more versatile definition of correction factors of flow rate, head and efficiency. They are calculated by the following equations.

$$f_Q = \frac{Q_v}{Q_w} \tag{II-1}$$

$$f_H = \frac{H_v}{H_w} \tag{II-2}$$

$$f_\eta = \frac{\eta_v}{\eta_w} \tag{II-3}$$

Some more correction factors were given based on the loss analysis, which includes the dissipation of the disk friction power. These corrections proved to be useful when compared with the experimental results of the pumps Gulich tested. In this study, the first two correction factors will be analyzed to verify the method as a way to study the effects of viscous fluids on ESPs.

A dimensionless analysis was performed by Timar [8] to study the performance of centrifugal pumps. Three dimensionless numbers were proposed, which are head coefficient, flow rate coefficient and the rotating Reynolds number. By the head results from experiments with a wide range of flow rates for service with water at difference rotation speed, a universal curve for centrifugal pumps working with water was obtained in Figure II-1.

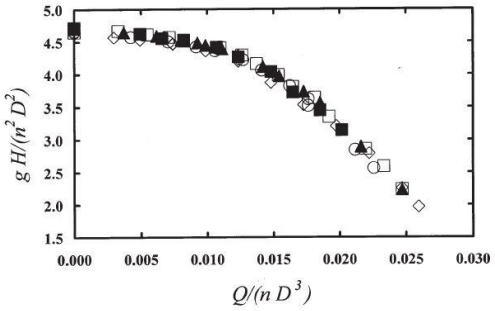

Figure II-1: Head coefficient as a function of flow rate coefficient for oil at various rotating speeds in centrifugal pumps [8]

In this figure, the curves for different Reynolds number match perfectly. Also, the product of flow coefficient and Reynolds number was introduced as another dimensionless number to study the influence of viscosity.

CFD is a popular method used to study rotational machinery in the last 20 years. Feng [9] performed CFD simulations on turbulence flow inside a pump to search the applicability of different models in unsteady flow. The author concluded the turbulence simulation models can be used to foresee the unsteady flow inside a radial pump. And there is no significant difference among the turbulence models in pressure related parameters.

Majidi [10] carried out a 3D flow simulation inside a pump volute. This paper proved the reliability of CFD codes for solving 3D viscous flow problems inside centrifugal pumps. Standard k-ε turbulence equation was used for solving the cases in Majidi's work.

Barrios [11] performed both single-phase and two-phase flow simulation on ESPs. As the CFD results were in consistent with experimental results, Barrios was able to explore numerically the flow field inside the ESP.

Muiltiphase flow inside an ESP is researched numerically by Marsis [12]. High GVF flow, which is a common problem of ESPs, is studied by CFD simulations in the research.

A dimensionless method was analyzed on the characteristics of pump performance. Stel [13] numerically searched the viscosity influences on ESP. Introduced a new equation to define Reynolds numbers; he discussed the effects of viscosity on

head degradation of the pump. Dimensionless numbers were employed in this research. For cases under different working conditions but the same Reynolds number, it was revealed that they have the same performance curve and efficiency.

Sirino [14] performed similar simulations with Stel [13] on the same pump. The flow field inside the pump was investigated. It is found that the streamlines inside the pump channels are not always bladed oriented.

III. OBJECTIVES

When pumping crude oil from offshore wells, high viscosity of the fluids usually depletes ESP head. To better understand the mechanism of the effects of viscosity on ESP performance, this research aims to use the CFD method to simulate the complex flow fields inside ESPs.

In order to lower simulation procedure complexity, simply one of the stages of a multistage pump is modelled and researched. Balance holes are neglected to reduce the calculation time and simplify the geometries. The tested ESP model is WJE-1000, manufactured by Baker Hughes. Gambit is adopted for the meshing task. Commercial CFD software ANSYS Fluent is used as the CFD solver. Post process and result analysis are performed in software Teclpot and CFD Post.

Single phase flow is the focus of this work to study the flow behaviors inside the pump. Transient state simulations should be carried out. The simulation results are to be compared to experimental results, seeking for good consistency. From the validated CFD model, flow dynamics in the pump channels can be comprehensively analyzed. Dimensionless analysis needs to be performed to better understand the performance characteristics of ESPs. Quantified viscosity related parameters of the performance of pump need to be found to search the way of improving ESP efficiency. Power related dimensionless numbers need to be calculated to investigate the performance curve of this pump.

IV. MODELLING PROCEDURE

IV.1. Electrical Submersible Pump (ESP)

The Baker Hughes Centrilift WJE-1000 is the ESP model studied in this work. This will be referred to as WJE-1000 in the remainder of this thesis. This is a three-stage centrifugal pump with mixed-flow type impellers. Figure IV-1 shows the suction view of the impeller. There are five blades in the impeller, along with five balance holes. In the simulation model, balance holes are removed for simplification.

Figure IV-1: Photo of the impeller of WJE-1000 [15]

Figure IV-2: Photo of the diffuser of WJE-1000 [15]

Figure IV-2 shows the discharge view of the diffuser. There are seven vanes in the diffuser. This is a relatively large pump as the diameter of the stage is 8.15”. The engineering drawings of the impeller and the diffuser are shown in Figure IV-3 and Figure IV-4 respectively. The dimensions and specifications of WJE-100 were measured by the experiment group in the author’s lab.

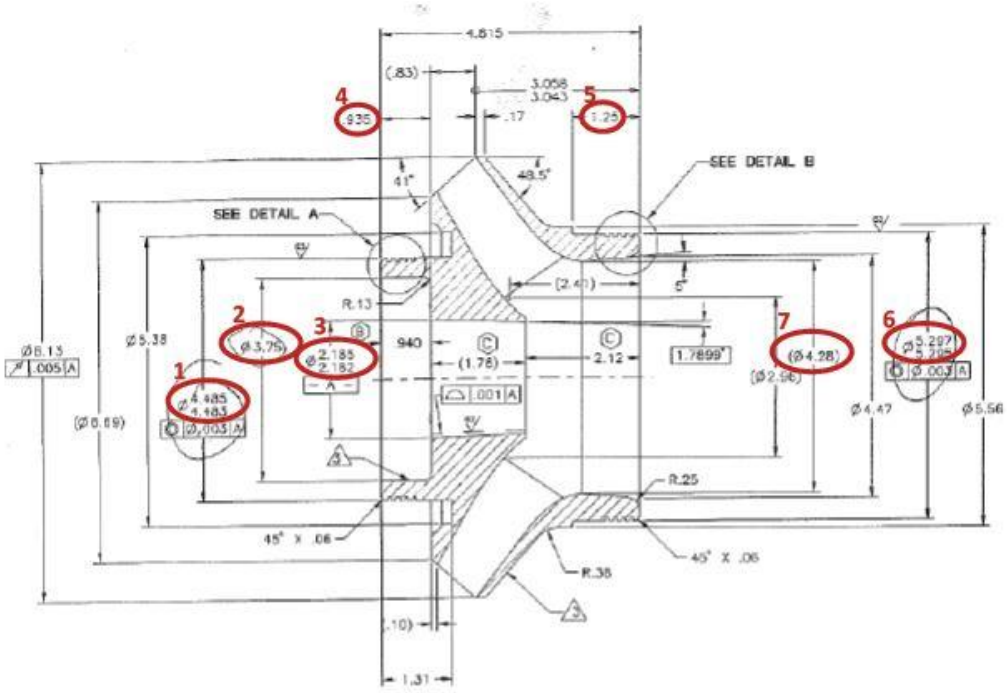

Figure IV-3: Dimensions of the impeller of WJE-1000 [15]

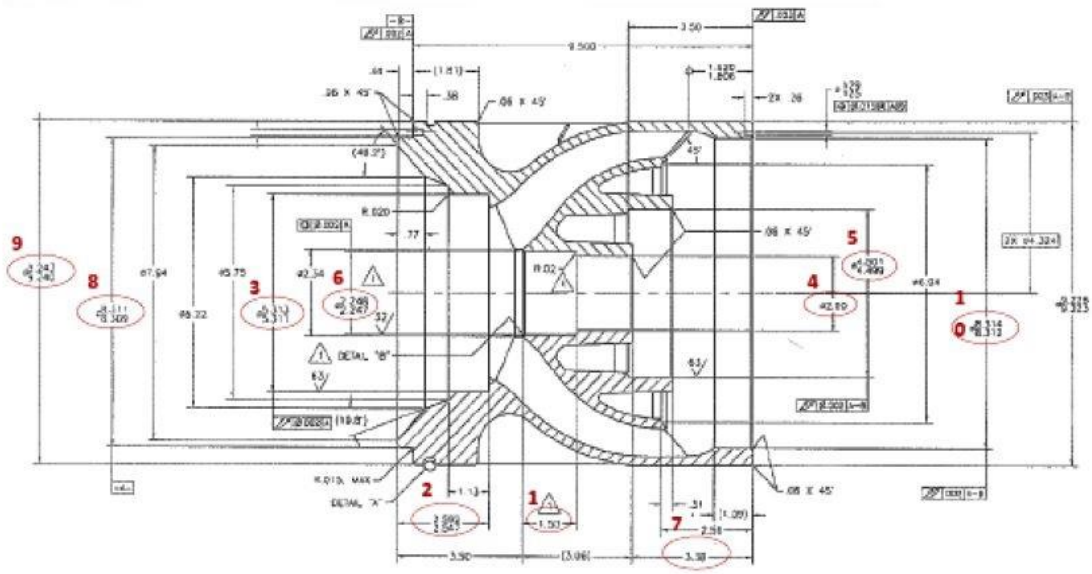

Figure IV-4: Dimensions of the diffuser of WJE-1000 [15]

The dimensions and specifications of the impeller and the diffuser are shown in Table IV-1. Capital letter D denotes to the diameter of a specified surface, while *h* and *t* refers to height and thickness respectively. The subscripts *1, 2, 3* and *4* mean impeller inlet, impeller outlet, diffuser inlet and diffuser outlet. Inner and outer are differentiated into subscript *i* and *o*.

Table IV-1: Dimensions and specifications of WJE-1000

Dimension	Impeller	Diffuser
Blades/Vanes	5 blades	7 vanes
Inlet inner diameter (mm)	$D_{1,i}$=48.2	$D_{3,i}$=183.0
Inlet outer diameter (mm)	$D_{1,o}$=116.5	$D_{3,o}$=218.6
Inlet blade height (mm)	h_1=35.0	h_3=19.8
Inlet blade hickness (mm)	t_1=4.8	t_3=3.8
Outlet inner diameter (mm)	$D_{2,i}$=183.0	$D_{4,i}$=48.2
Outlet outer diameter (mm)	$D_{2,o}$=218.6	$D_{4,o}$=116.5
Outlet blade height (mm)	h_2=24.8	h_4=22.9
Outlet blade thickness (mm)	t_2=2.1	t_4=4.8

According to the pump catalog as shown in Figure IV-5, WJE-1000 delivers a flow rate of nearly 1,100 gallons per minute (gpm) with a pressure rise of 150psi by the whole three stages at the best efficiency point (BEP) at a rotational speed of 3600 rpm.

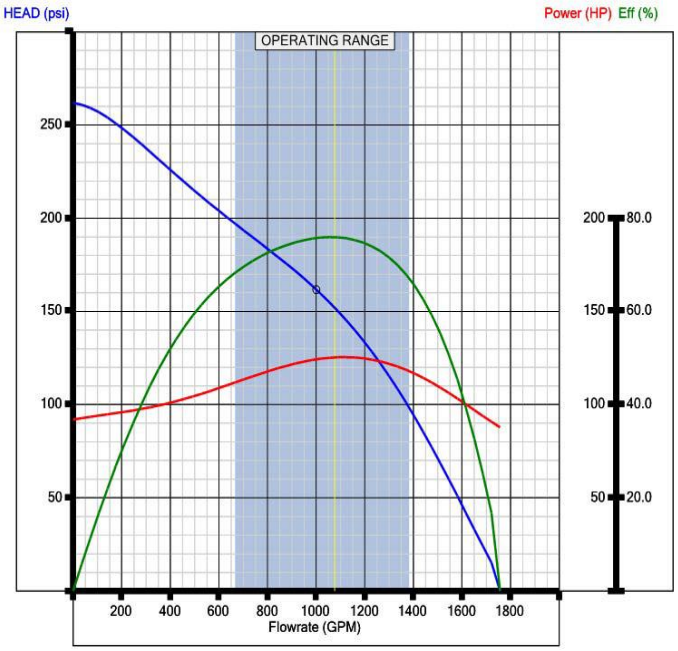

Figure IV-5: Catalog performance curve of WJE-1000 at 3600 rpm [15]

IV.2. Model and Mesh

The CAD model of WJE-1000 was acquired by the Turbomachinery Lab. A single stage including one impeller and one diffuser was investigated in this research. Figure IV-6 shows the CAD models of the impeller in Figure IV-6(a) and the diffuser in Figure IV-6(b).

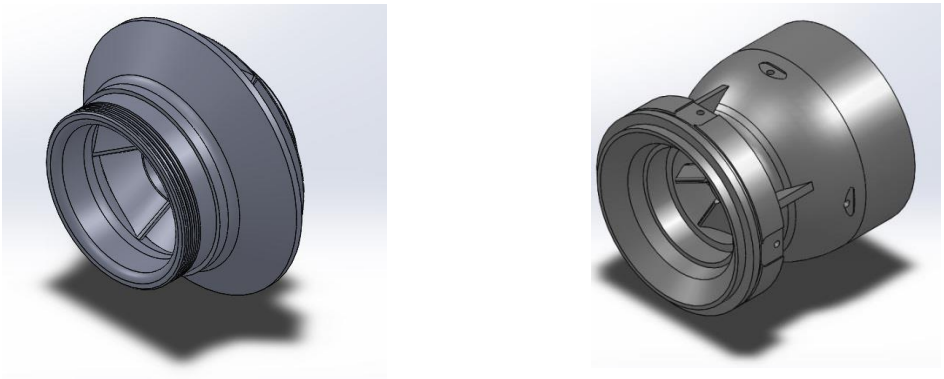

(a) (b)

Figure IV-6: CAD models of the impeller and the diffuser of WJE-1000

The geometries of WJE-1000 are too complex to simulate in CFD software. Simplification on the CAD model was performed to make it possible for calculation. All five balance holes in the impeller were eliminated to reduce the complexity.

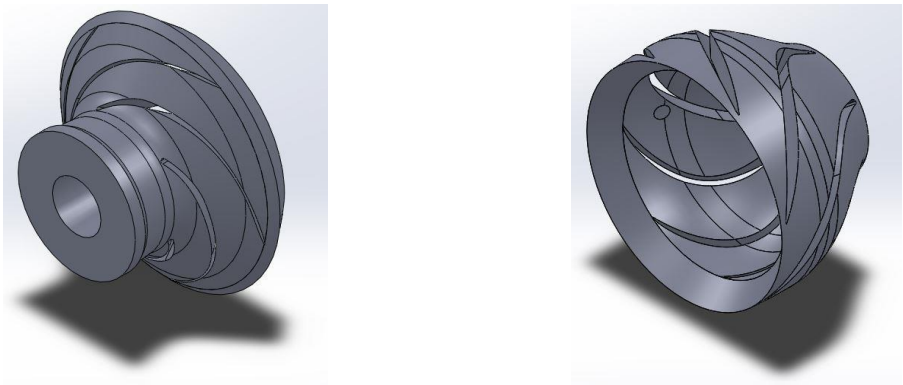

(a) (b)

Figure IV-7: Simplified models of the impeller and the diffuser

Figure IV-7 are the views of the simplified models of the impeller and diffuser respectively. The secondary flow paths were not modelled so to increase the calculation efficiency. All the seal leakage was not included in this study.

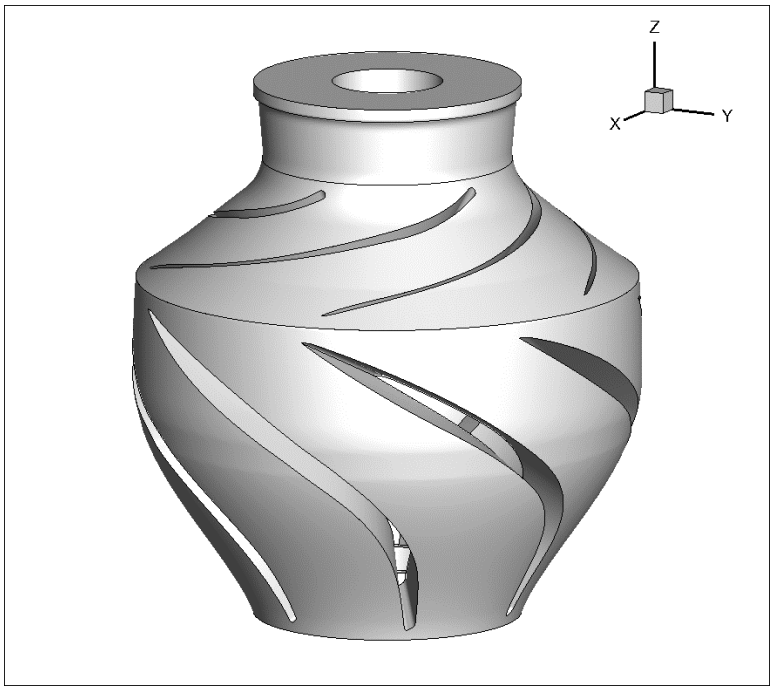

Figure IV-8: Final model of the stage of the pump

Figure IV-8 shows the final model of the whole single stage of WJE-1000 in Tecplot. The upper side of the model is the inlet of the stage while the bottom is the discharge of the diffuser. To improve numerical stability for the simulations, a specified flow rate value was imposed at the inlet of the impeller. The direction of the flow rate is perpendicular to the face of the inlet. A fixed value reference pressure was set at the discharge of the diffuser to enhance the calculation quality.

All the surfaces in the model were treated as no slip walls. All the clearance, such as the clearance between the impeller and the diffuser and the gaps around hubs, were ignored in the model. Software Gambit was employed to perform the meshing task of the model. In order to reduce the total number of nodes, this thesis used hexahedral elements rather than tetrahedral elements. Regions such as the blades and the edges were especially refined for better calculation accuracy. The total number of nodes is 6.76 million for the whole stage, including both the impeller and the diffuser. Then the mesh was exported to ANSYS Fluent for solving. Figure IV-9 shows the grid of model of WJE-1000.

Figure IV-9: Illustration of the mesh of the whole stage

The structured mesh shows good refinement in critical areas such as the blades and the hubs. Near wall mesh work was inspected to verify that y^* is low enough in every sub domain.

IV.3. Grid Independence Study

A grid independence study was performed to investigate the influence of number of nodes on the simulation result. The result of the independence study proves that the variation in hydraulic head between the original model and the refined model is negligible.

To study the effect of node numbers, the original grid was more detailed meshed. The total number of nodes rises to 8.6 million from the primary 6.8 million. Figure IV-10 (a) shows the original mesh view of the impeller blades and shoulder. Figure IV-10 (b) shows the refined mesh view of the impeller blades and shoulder. In comparison, the grid in refined mesh is more detailed in critical parts than the grid in original mesh. In fact, the mesh in all parts of the stage was refined.

(a) (b)

Figure IV-10: Comparison of the original mesh and the refined mesh

The results of both models are concluded in Table IV-2. In the final results, the area average pressure at the inlet is similar to each other. After the grid refinement, the pressure rise of the stage changes merely 0.07%. This proves the influence of adding the number of nodes on the simulation result is negligible. Thus the original grid is independent of the number of nodes. The original grid was used for all the remaining CFD simulations as the correct mesh.

Table IV-2: Comparison of the results between the original mesh and the refined mesh in grid independence study

	Original mesh	Refined mesh
Number of nodes	6763011	8609436
Pressure outlet (fixed value) (Pa)	414000	414000
Pressure inlet (Pa)	-44960	-45289
Pressure rise (Pa)	458960	459289
Pressure rise (psi)	66.57	66.61

V. SIMULATION SETUP

V.1. Reynolds Number

To classify the flow regimes under all operation conditions in this work, the definition of Reynolds number has to be discussed. There is no literature which provides a precise methodology in determining Reynolds number for ESPs. Sun [16] presented a formulation of Reynolds number concerning the cross section shape effect, system rotation and channel curvature. But the effects of these parameters were studied separately in simply geometry cases. The combined influence on the modification of Reynolds number is unknown. And the models studied are not validated with experimental results in the research. Stel [13] posed a reasonable equation for the Reynolds number for ESPs. It is based on the inlet cross section area and inlet hydraulic diameter. This is not a comprehensive methodology because transitional regimes are not studied in Stel's work. Although a rough estimation, the results using this equation as the calculation of Reynolds number shows good consistency with experimental results. The Reynolds number calculation is Eq. (V-1).

$$Re_{Dh} = \frac{(Q/A_{in}) \cdot D_h \cdot \rho}{\mu} \tag{V-1}$$

Q is the flow rate of the pump, A_{in} is the inlet cross section area, D_h is the hydraulic diameter at the inlet, ρ is the density of testing fluid and μ is the viscosity of the fluid. In this model, the hydraulic diameter is decided by Eq. (V-2). $D_{1,o}$ is the impeller outlet diameter and $D_{1,i}$ is the impeller inlet diameter.

$$D_h = D_{1,o} - D_{1,i} \quad \text{(V-2)}$$

Based on Stel's theory [13], cases with Reynolds number larger than 2300 are treated as being in the turbulence flow regime. Cases with Reynolds number less than 2300 are treated as being in the laminar flow regime.

However, as the definition is rather superficial, some cases with Reynolds number less than 2300 were still regarded as turbulence flow in this study. In fact, it is very difficult to infer on the flow regime in the whole stage pump with complex impeller and diffuser geometries.

V.2. Solving Model

For the turbulence flow, the standard $k-\epsilon$ two equations model was utilized in the Fluent software [17]. This model is based on the Reynolds Averaged Navier-Stokes Equations (RANS). The transport equations in RANS are shown in Eq. (V-3) and Eq. (V-4).

The turbulent kinect energy equation for *k* is calculated as following.

$$\frac{\partial}{\partial t}(\rho k) + \frac{\partial}{\partial x_i}(pku_i) = \frac{\partial}{\partial x_j}\left[(\mu + \frac{\mu_t}{\sigma_k})\frac{\partial k}{\partial x_j}\right] + G_k + G_b - \rho\epsilon - Y_M + S_k \quad \text{(V-3)}$$

For the dissipation rate ϵ is the following equation.

$$\begin{aligned} &\frac{\partial}{\partial t}(\rho\epsilon) + \frac{\partial}{\partial x_i}(\rho\epsilon u_i) \\ &= \frac{\partial}{\partial x_j}\left[(\mu + \frac{\mu_t}{\sigma_\epsilon})\frac{\partial \varepsilon}{\partial x_j}\right] + C_{1\epsilon}\frac{\epsilon}{k}(G_k + C_{3\epsilon}G_b) - C_{2\epsilon}\rho\frac{\epsilon^2}{k} + S_\epsilon \end{aligned} \quad \text{(V-4)}$$

In the equations, G_k is the turbulence kinect energy generated by the mean velocity gradient. The equation to calculate G_k is Eq. (V-5).

$$G_k = -\rho\overline{u_i' u_j'}\frac{\partial u_j}{\partial x_i} \tag{V-5}$$

Under Boussinesq's assumption, G_k is revised as the following definition in (V-6).

$$G_k = \mu_t S^2 \tag{V-6}$$

In the Eq. (V-7), S is the coefficient and defined as.

$$S = \sqrt{2S_{ij}S_{ij}} \tag{V-7}$$

G_b in the transport equations is the turbulence kinect energy generated by buoyancy. The equation to calculate G_b is Eq. (V-8).

$$G_b = -g_i \frac{\mu_t}{\rho P_{rt}} \frac{\partial \rho}{\partial x_i} \tag{V-8}$$

In the Eq. (V-8), P_{rt} is the Prandtl number for turbulence energy and g_i is the gravity, and β is the coefficient of thermal expansion. The calculation for β is as follows.

$$\beta = -\frac{1}{\rho}\left(\frac{\partial \rho}{\partial T}\right)_p \tag{V-9}$$

Y_M is the dissipation generated from compressible turbulence. In this study, it is not included. $C_{1\epsilon}$, $C_{2\epsilon}$ and $C_{3\epsilon}$ are model constants. σ_k and σ_ε are the turbulent Prandtl numbers for equation k and equation ε. S_k and S_ε are user defined source terms.

The turbulence viscosity is decided by k and ϵ. The equation is as followed.

$$\mu_t = \rho C_\mu \frac{k^2}{\varepsilon} \tag{V-10}$$

C_μ is the model constant.

In this study, all the constants are set as Fluent default setting. All these values are acquainted by experience from practice.

$$C_\mu = 0.09 \tag{V-11}$$

$$C_{1\varepsilon} = 1.44 \tag{V-12}$$

$$C_{2\varepsilon} = 1.92 \tag{V-13}$$

$$C_{3\varepsilon} = 1.3 \tag{V-14}$$

$$\sigma_k = 1.0 \tag{V-15}$$

$$\sigma_\varepsilon = 1.3 \tag{V-16}$$

The near wall areas are treated with the standard wall functions in this model. The equations are based on the assumptions of Launder and Spalading, and employed widely in flow simulation. The equation for mean velocity area is Eq. (V-17).

$$U^* = \frac{1}{\kappa} ln(Ey^*) \tag{V-17}$$

In this equation, U^* and y^* are defined as follows.

$$U^* = \frac{U_P C_\mu^{1/4} k_P^{1/2}}{\tau_w/\rho} \tag{V-18}$$

$$y^* = \frac{\rho C_\mu^{1/4} k_P^{1/2} y_P}{\mu} \tag{V-19}$$

k is the von Karman constant and equals to 0.42 in this model. E is the empirical constant and equals to 9.81. U_P is the mean velocity of the particle at point P. k_P is the turbulence kinect energy at point p. This logarithm is valid for 30 < y^* <60. When the y^*<11.225, the Fluent software uses stress-strain model in which $U^* = y^*$.

For the operating conditions treated as laminar flow, the laminar model was utilized in Fluent software. The unsteady N-S equations were adopted for laminar flow. The non-dimensional form of the unsteady incompressible N-S equations is shown as follows.

$$\frac{\partial \rho}{\partial t} + \nabla \cdot \rho \overrightarrow{v_r} = 0 \tag{V-20}$$

$$\frac{\partial}{\partial t}\rho \vec{v} + \nabla \cdot (\rho \overrightarrow{v_r} \vec{v}) + \rho(\vec{w} \times \vec{v}) = -\nabla p + \nabla \vec{\tau} + \vec{F} \tag{V-21}$$

$$\frac{\partial}{\partial t}\rho E + \nabla \cdot (\rho \overrightarrow{v_r} H + \rho \overrightarrow{u_r}) = \nabla \cdot (k \nabla T + \vec{\tau} \cdot \vec{v}) + S_h \tag{V-22}$$

These are the equations for a rotating frame for absolute velocity in Fluent software. Eq. (V-20) is the conservation of mass equation. Eq. (V-21) is the conservation of momentum equation. Eq. (V-22) is the conservation of energy equation.

V.3. Testing Fluids

In order to study the influence of viscosity on the ESP, numerous simulations under different operation conditions were conducted.

Six groups of different viscosity and density fluids were simulated under seven various working conditions. The material for the first group is pure water. It is chosen to validate with the experimental results. Other five groups were conducted by the same oil of different viscosities. The chosen oil is Conosol C-200 [18]. All working conditions are summarized in the Table V-1, Table V-2, Table V-3, Table V-4, Table V-5 and Table V-6.

Table V-1: Properties and simulation conditions for pure water

Case	Material	Viscosity (cP)	Density (kg/m^3)	Flow rate (gpm)	Reynolds number
1.1	Water	1	998.2	437.5	212963.9
1.2	Water	1	998.2	583.4	283947.7
1.3	Water	1	998.2	729.1	354884.6
1.4	Water	1	998.2	875.0	425921.6
1.5	Water	1	998.2	1020.9	496908.5
1.6	Water	1	998.2	1166.7	567895.4
1.7	Water	1	998.2	1312.5	638882.4

Table V-2: Properties and simulation conditions for 2.4cP oil

Case	Material	Viscosity (cP)	Density (kg/m^3)	Flow rate (gpm)	Reynolds number
2.1	C-200	2.4	818.4	533.6	88734.9
2.2	C-200	2.4	818.4	711.5	118311.5
2.3	C-200	2.4	818.4	889.3	147868.6
2.4	C-200	2.4	818.4	1067.3	177467.3
2.5	C-200	2.4	818.4	1245.2	207045.2
2.6	C-200	2.4	818.4	1423.0	236623.1
2.7	C-200	2.4	818.4	1600.9	266201.0

Table V-3: Properties and simulation conditions for 10cP oil

Case	Material	Viscosity (cP)	Density (kg/m^3)	Flow rate (gpm)	Reynolds number
3.1	C-200	10	818.4	533.6	21296.4
3.2	C-200	10	818.4	711.5	28394.8
3.3	C-200	10	818.4	889.3	35488.4
3.4	C-200	10	818.4	1067.3	42592.2
3.5	C-200	10	818.4	1245.2	49690.8
3.6	C-200	10	818.4	1423.0	56789.5
3.7	C-200	10	818.4	1600.9	63888.2

Table V-4: Properties and simulation conditions for 60cP oil

Case	Material	Viscosity (cP)	Density (kg/m^3)	Flow rate (gpm)	Reynolds number
4.1	C-200	60	818.4	533.6	3549.4
4.2	C-200	60	818.4	711.5	4732.5
4.3	C-200	60	818.4	889.3	5914.7
4.4	C-200	60	818.4	1067.3	7098.7
4.5	C-200	60	818.4	1245.2	8281.8
4.6	C-200	60	818.4	1423.0	9464.9
4.7	C-200	60	818.4	1600.9	10648.0

Table V-5: Properties and simulation conditions for 200cP oil

Case	Material	Viscosity (cP)	Density (kg/m^3)	Flow rate (gpm)	Reynolds number
5.1	C-200	200	818.4	533.6	1064.8
5.2	C-200	200	818.4	711.5	1419.7
5.3	C-200	200	818.4	889.3	1774.4
5.4	C-200	200	818.4	1067.3	2129.6
5.5	C-200	200	818.4	1245.2	2484.5
5.6	C-200	200	818.4	1423.0	2839.5
5.7	C-200	200	818.4	1600.9	3194.4

Table V-6: Properties and simulation conditions for 400cP oil

Case	Material	Viscosity (cP)	Density (kg/m^3)	Flow rate (gpm)	Reynolds number
6.1	C-200	400	818.4	533.6	532.
6.2	C-200	400	818.4	711.5	709.9
6.3	C-200	400	818.4	889.3	887.2
6.4	C-200	400	818.4	1067.3	1064.8
6.5	C-200	400	818.4	1245.2	1242.3
6.6	C-200	400	818.4	1423.0	1419.7
6.7	C-200	400	818.4	1600.9	1597.2

The properties of pure water are decided by the default values in the material database of Fluent software, of which viscosity is 0.001 kg/m-s and density is 998.2 kg/m^3. The density of C-200 oil is obtained from the manufacture [18]. The change in density of oil due to the temperature change is neglected in this study. Five different values of the viscosities of C-200 oil, which are 2.4cP 10cP 60cP 200cP and 400cP, were chosen among the normal range of viscosity of the oil under ordinary working conditions. The flow rates for service with water were chosen to follow the experiment conditions on WJE-1000. Flow rates for service with C-200 oil were chosen accordingly.

During the procedure of experiments, the viscosity of oil will drop dramatically as the working temperature rises. The change in viscosity will make simulations extremely difficult. In this study, to better understand the effects of viscosity, all the values of viscosity of test fluids are set as fixed for simplification. So the impact of temperature change inside the pump is not included in the results.

The Reynold number is the tables is calculated by the Eq. (V-1). In the equation, Q is the inlet flow rate as shown in different cases. A_{in} is the cross section area at the inlet. In the model of WJE-1000, the area is 0.00885 m^2 as measured in the chapter 4. D_h is the hydraulic diameter of the inlet. For the stage of the pump, the inlet has an annulus shape surface. The hydraulic diameter is decided by Eq. (V-2). In this model, the outer diameter $D_{1,o}$ is 116.6 mm and inner diameter $D_{1,i}$ is 48.2 mm, so the hydraulic diameter of the model is 68.4 mm in all cases.

Based on literatures, when Reynolds number is larger than 2300, the flow regime is treated as turbulence. In this research, all the cases with viscosity less than 200cP,

were simulated as turbulence flow. In the cases 6.1-6.6, of which fluid viscosity is 400cP, Reynolds numbers are all less than 1600, which were treated as laminar flow.

The difficulty is how to define the flow regimes in 200cP oil cases as the Reynolds numbers are approaching 2300. In fact, the complexity of the impeller and diffuser geometries makes it hard to offer a precise method to identify the flow regimes. Thus in this work, the turbulence model was used in all cases of 200cP oil for the sake of consistency.

V.4. Boundary Conditions and Time Step

Transient simulations were performed to study the flow behavior inside the pump. As boundary condition, a specified liquid flow rate was imposed at the inlet of the stage. A fixed reference pressure of p=100psi was set at the outlet of the stage. Zero psi was entered as the initial inlet pressure. It is simply a starting value and does not affect the final flow fields and pressure distribution.

The impeller and inlet inner walls were considered as rotational wall. Diffuser was regarded as a stationary part. The rotational speed in this study was set as 3600 rpm according to the pump catalog. All the walls were treated as no-slip walls. In the impeller flow domain, transient effects were simulated by using moving mesh option.

In all simulations, every time step is set by one degree. Since the rotational speed is 3600 rpm, the time step size is then 4.62963×10^{-5} second. In a time step sensibility test, the time step was set as half degree to study the influence of the time step size, which is 2.31×10^{-5} second. For all the performance quantities investigated, discrepancies

between the results are less than 1%. The sensibility test proved that the span of 4.62963×10^{-5} second for time step is reasonable in this pump model.

To achieve the convergence criterion of RMS residual below 10^{-5}, the total number of time steps was studied. During the calculations, cases with lower viscosity and lower inlet flow rate tend to be unstable, and need more time steps. With the sensibility analysis and the proof of simulation tests, all cases need no more than 798 time steps for the inlet pressure to achieve its periodicity.

VI. RESULTS AND DISCUSSION

VI.1. Pump Performance

The most important performance quantity of a pump is the pressure rise (hydraulic head). In this study, the pressure at the outlet of the stage was set as a constant value of 100psi for reference in all cases. When the simulation reached its periodicity and the RMS residual went below 10^{-5}, the pressure at the inlet was recorded for calculation. Figure VI-1(a) shows the position of inlet pressure in the model. Figure VI-1(b) shows the position of outlet pressure in the model.

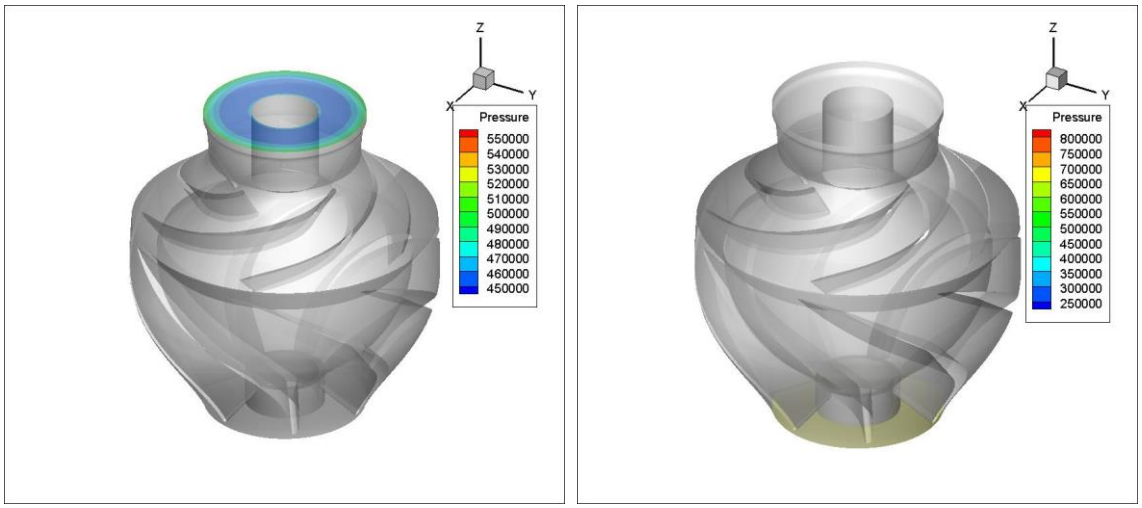

(a) (b)

Figure VI-1: Illustration of the positions of inlet pressure and outlet pressure in the model

Figure VI-2(a) is the 2-D view of the pressure contour at the inlet. Figure VI-2(b) is the pressure contour at the outlet. In Figure VI-2(b), the whole area has the same pressure at the outlet as it was set to be constant. In Figure VI-2(a), since the pressure at the inlet is different at various points, the area-weighted average pressure at the inlet cross section was adopted as the value of the inlet pressure. This method will be used for the following pressure measurements as well.

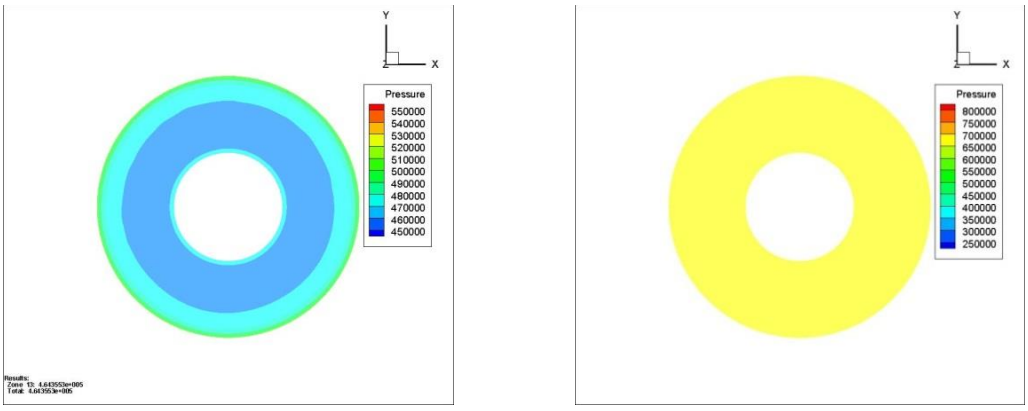

(a) (b)

Figure VI-2: 2D views of the pressure contour at inlet and outlet of the stage

Then the pressure rise of the whole stage is calculated as the pressure at the discharge of the diffuser minus the area-weighted average pressure at the inlet.

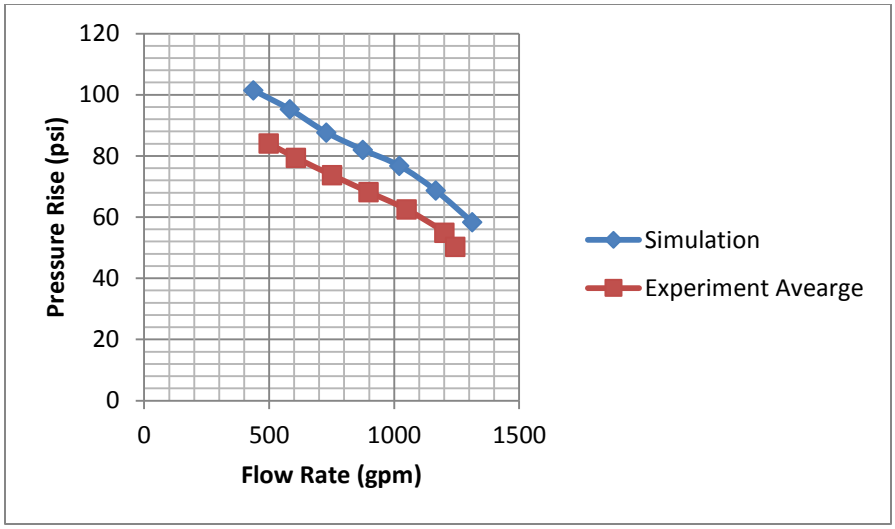

Figure VI-3: Comparison of the pressure rises in psi between the simulation results and the experimental results for pure water (1cP) [19]

Figure VI-3 is the comparison for pure water between simulation results and experimental results. The Y-axis represents the pressure rise of the whole single stage; and unit is psi. The X-axis is the flow rate in gpm in every case.

The two lines in Figure VI-3 are not the same. There are a couple of reasons for the deviation.

First of all, all the results for the experiments are the average pressure rise of a whole three-stage pump. In reality, the pressure rises are not the same in every stage. Normally, since the inlet flow is strong and unstable, the first stage of the pump has the lowest hydraulic head. In this CFD model, the flow at the inlet is simulated as normal to the inlet and is a stable flow field. Thus the hydraulic head of simulations should be better than the average of multistage experimental results. Due to the lack of data, there is no correct experimental result of the pressure rise of a single stage.

Secondly, as mentioned above, all five balance holes in the impeller are neglected in the model. In experiments, due to the reflux and other effects, the balance holes will contribute to the hydraulic head negatively inside the pump. This might be main reason for the discrepancy of the two curves in Figure VI-3.

The last but not lease, the leakage and secondary flow are not taken into consideration in this study. From experiments and literatures, these effects will also lower the pressure performance of the pump.

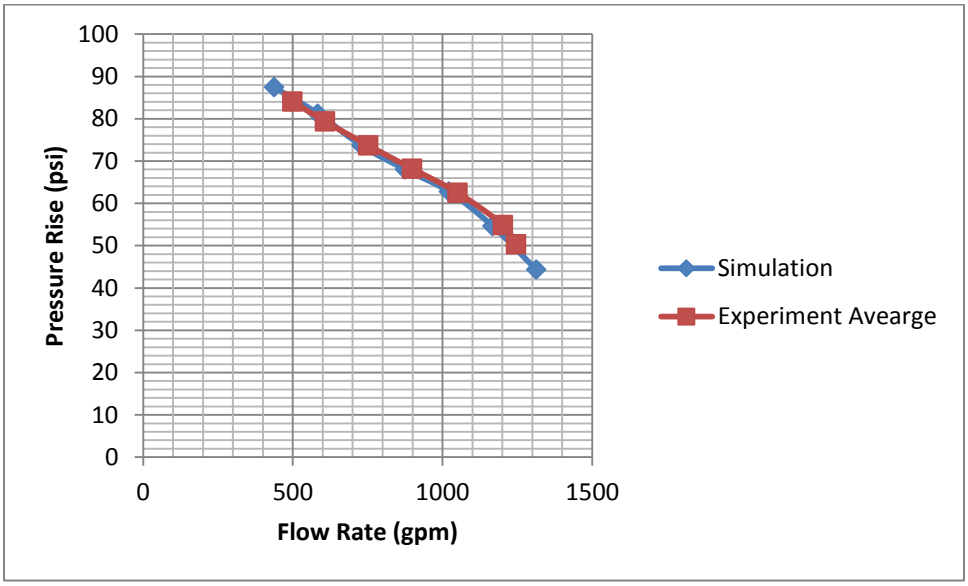

Figure VI-4: Modified comparison of the pressure rises in psi between the simulation results and the experimental results for pure water (1cP)

Due to the lack of data and simplification, a modified comparison between simulation results and experimental results is given in Figure VI-4. The result of simulation in every case is reduced by 14 psi which results in the simulations fitting the

curve of experimental results. The two curves in Figure VI-4 fit well. In the modified comparison, better agreement is observed in higher flow rate cases. Deviation is less than 1.1% for cases at a flow rate of 730 gpm or higher. Largest discrepancy 3.5% is noted in the case at a flow rate of 437 gpm. As Feng [9] discussed, turbulence models cannot simulate all flow features in strong part-load conditions. In this way, CFD results in part-load cases are not as accurate as in over-load cases. Although not a precise manner, the two fitting curves in Figure VI-4 show good consistency, validating the model of WJE-1000.

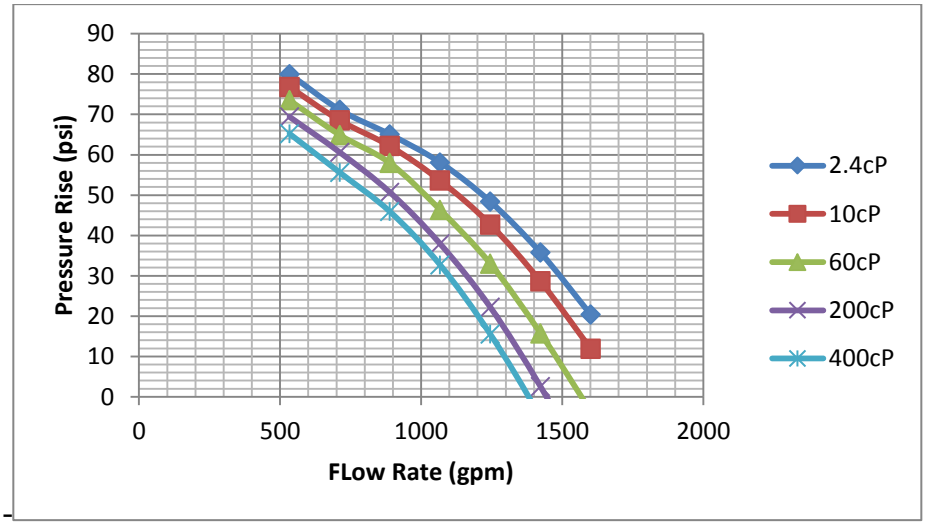

Figure VI-5: Pressure rises for different viscosity oils

Figure VI-5 summaries the results of pressure rise for service with different viscosity oils. In Figure VI-5, one can observe that the head performance is highest in the lowest flow rate condition for every fluid. As flow rate goes up, the pressure rise

declines for every group of oil cases. When the flow rate is increasing, the velocity of inlet flow is raising as well. The added velocity leads to higher shearing force of the fluids and higher energy loss. Thus the pressure rise is lower for cases at higher flow rate. Viscosity of the fluids has the same way of influence on the pump performance. When pumping highly viscous fluid, the strong shearing force results in more pressure loss than in low viscous cases. Detailed discussions about the influence of viscosity on the pump performance are in performance analysis part.

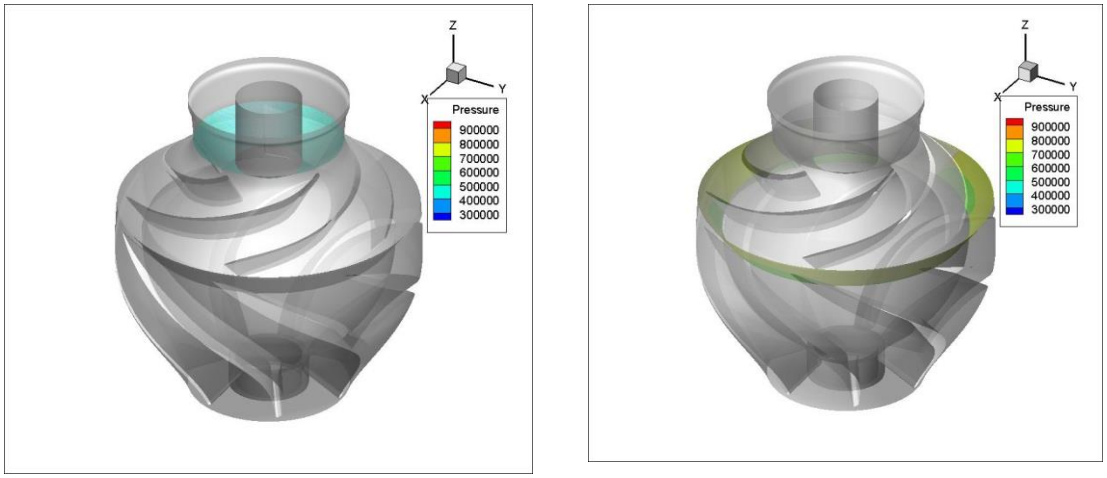

(a) (b)

Figure VI-6: Illustration of the positions of the impeller entrance and exit

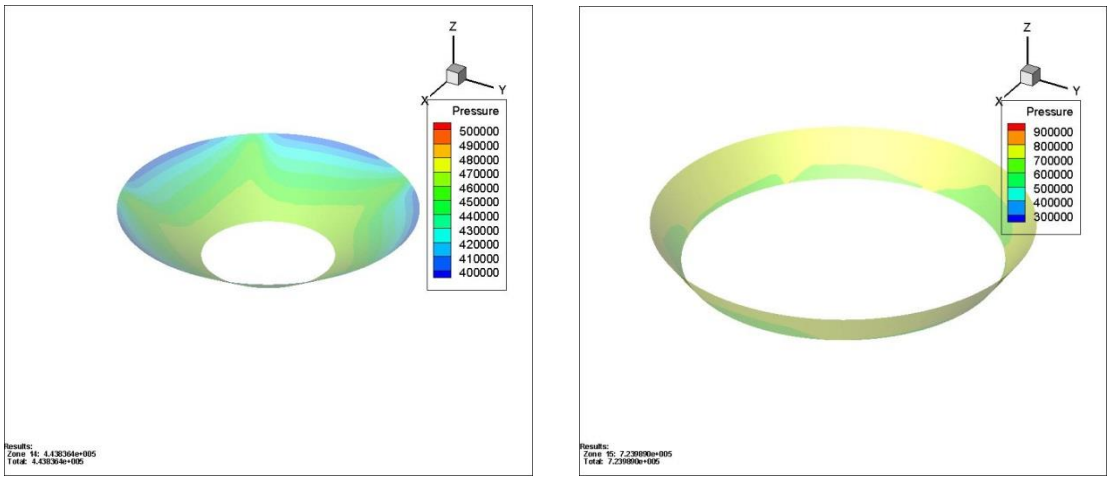

(a) (b)

Figure VI-7: Pressure contour views at the impeller entrance and exit

The pressure differences in the impeller and diffuser are investigated respectively in this research. Figure VI-6(a) shows the position of the entrance of the impeller in the model and Figure VI-6(b) shows the position of the exit of the impeller in the model. Figure VI-7(a) is the view of pressure contour at the entrance and Figure VI-7(b) is at the exit. In the impeller, the fluids enter at the exit of the inlet and leave the impeller at the entrance of the diffuser (the same as the impeller exit). The pressure rise in the impeller for different viscosity oils is shown in Figure VI-8.

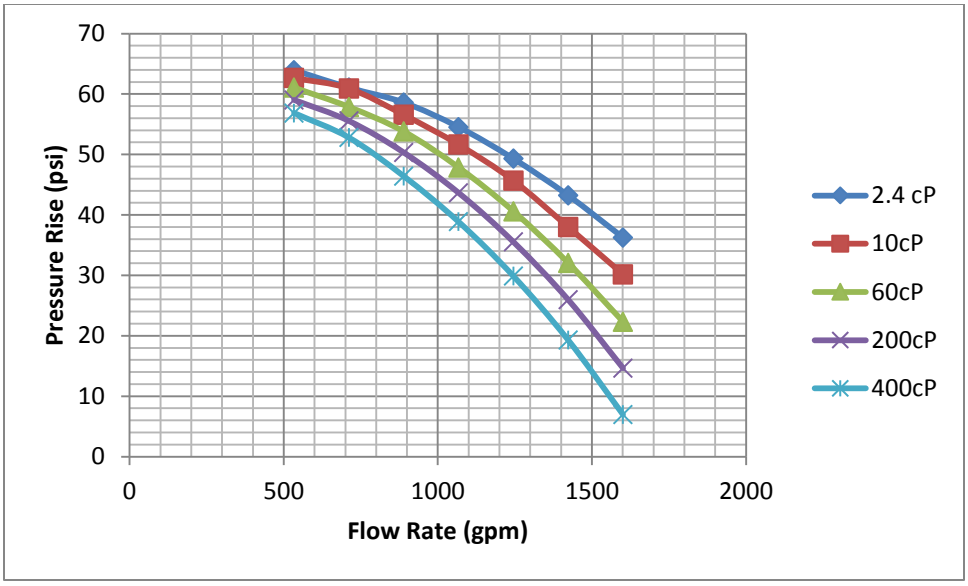

Figure VI-8: Pressure rises in the impeller for different viscosity oils

The pressure rise in the impeller is similar to the pressure change of the whole stage. The difference is that the curves in Figure VI-5 are steeper than the ones in Figure VI-8. This suggests the performance of the impeller is not as sensitive to flow rate as the whole stage. A detailed calculation shows the same conclusion regarding the influence of viscosity. For the whole stage, the pressure rise drops from 56 psi to 30 psi when replacing 2.4cP oil with 400cP oil at a flow rate of 1100 gpm. In the impeller between the same two flow rates, the degradation in pressure rise is only 18 psi. The comparison in viscosity and flow rate change indicates that the performance of the impeller has less viscosity dependence than the whole stage.

The discrepancy between the hydraulic head of the impeller and the whole stage is caused by the pressure change inside the diffuser as shown in Figure VI-9. The entrance of the diffuser is the same as exit of the impeller in Figure VI-6(b) and the exit

of the diffuser is the stage outlet as shown in Figure VI-1(b). The curves in Figure VI-9 prove that the diffuser is not always a pressure gain device. Even in pure water cases, the diffuser contributes to the pressure rise negatively at over-load flow rates. For high viscosity fluids, the diffuser starts to cause pressure loss in part-load conditions. When pumping 200cP oil at a flow rate of 1600 gpm, the pressure loss inside the diffuser is higher than the pressure rise in the impeller, which disables the pump.

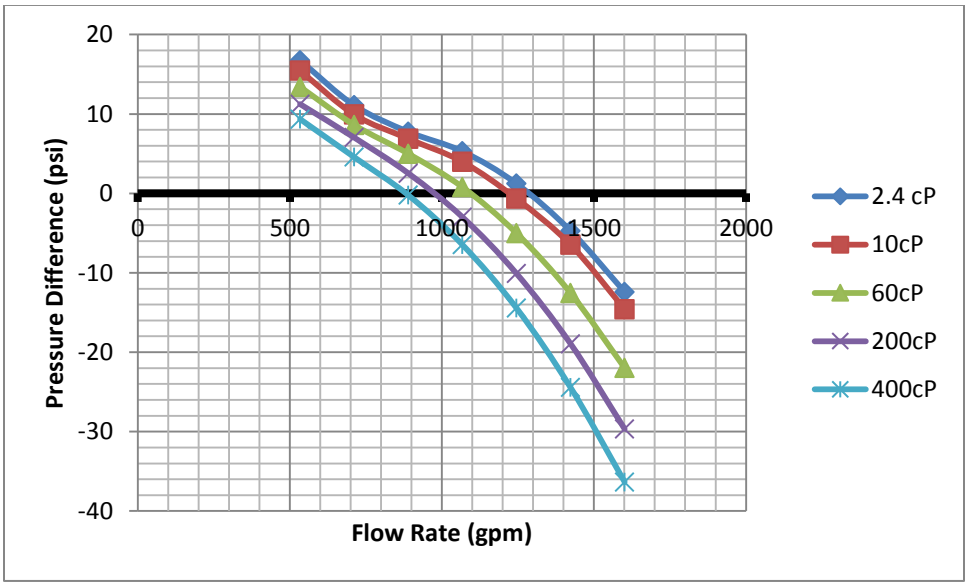

Figure VI-9: Pressure differences in the diffuser for different viscosity oils

The pressure change in both the impeller and the diffuser fits well with the head performance of the whole stage. A little deviation is caused by a small pressure drop in the inlet of the stage, which is regarded as an independent part of the model.

VI.2. Flow Analysis

The flow field in the pump channels was analyzed by the software CFD-Post. An overall view of the streamlines inside the pump in case 1.1 is shown in Figure VI-10.

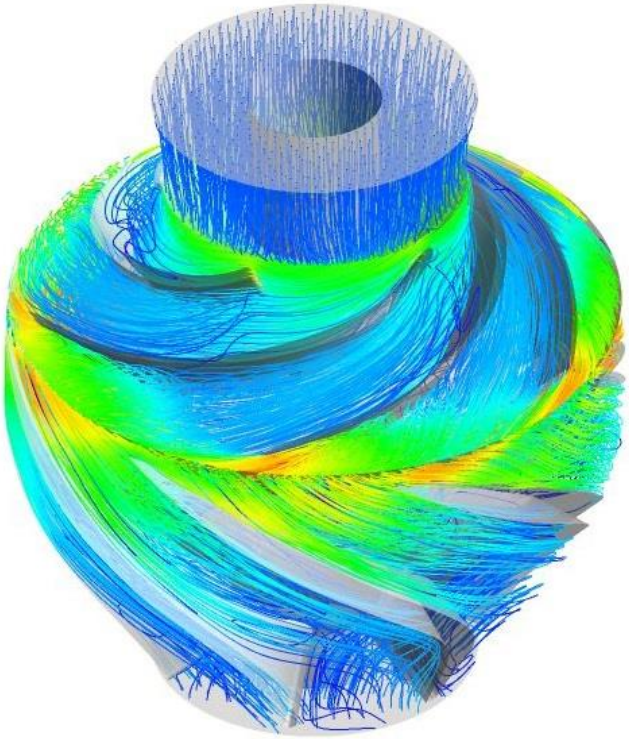

Figure VI-10: Streamlines inside the stage at a flow rate of 437.5 gpm for service with water (1cP)

In this figure, all the blades and hubs are set as transparent to allow visualization while keeping illustrating the position. All the shrouds are hidden in the same way. The color scale is a render for local velocity of the fluid.

Figure VI-11(a) is the streamlines in the impeller in case 1.1. Figure VI-11(b) is the streamlines in the diffuser in case 1.1. Large recirculation regions exist in both the impeller and diffuser in this case.

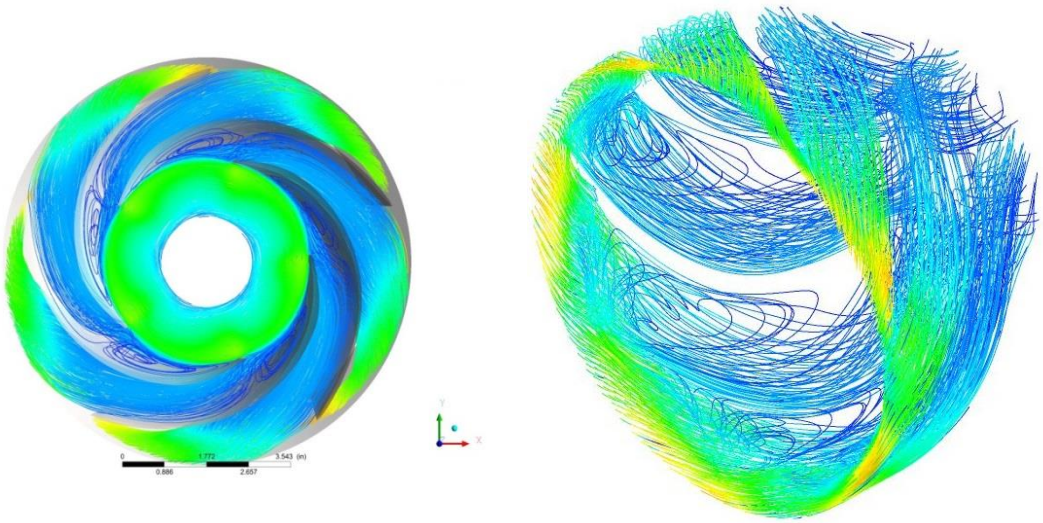

(a) (b)

Figure VI-11: Streamlines in the impeller (a) and diffuser (b) at a flow rate of 437.5 gpm for service with water (1cP)

When pumping the same fluid, the recirculation zones will reduce at higher flow rates. Figure VI-12 shows the streamlines in the impeller in Figure VI-12(a) and in the diffuser in Figure VI-12(b) in case 1.5. This case is chosen as the flow rate is 1021 gpm, which is close to the BEP. No measurable recirculation regions are found in the impeller. The recirculation spots in the diffuser become much smaller than in case 1.1.

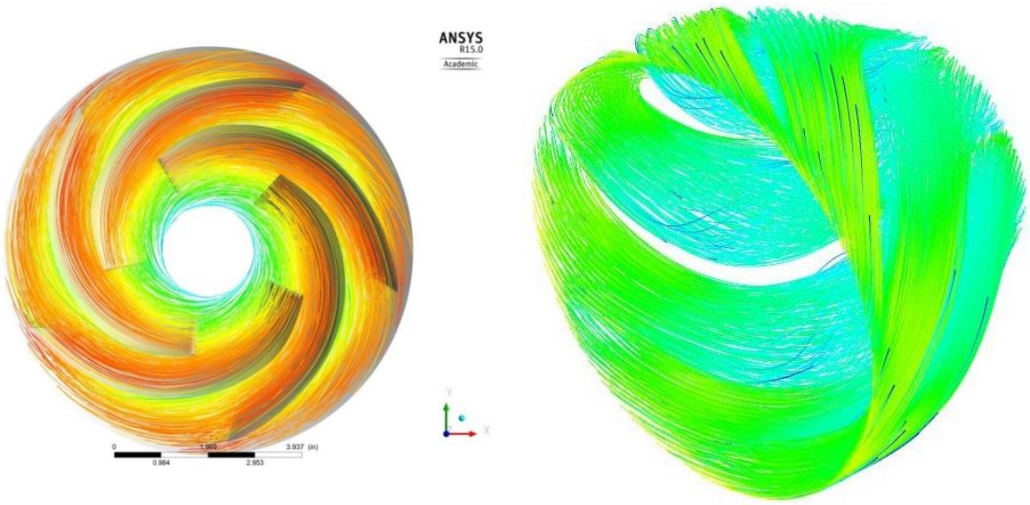

(a) (b)

Figure VI-12: Streamlines in the impeller (a) and diffuser (b) at a flow rate of 1021 gpm for service with water (1cP)

To study the influence of viscosity on the flow fields inside the pump, the streamlines in case 5.1, for service with 200cP oil at a similar flow rate with case 1.1, are shown in Figure VI-13. Recirculation zones can still be observed in part-load conditions when pumping high viscosity fluids. Compare with case 1.1, recirculation spots are decreasing in both quantity and size. The streamlines in Figure VI-13 are more uniform than in Figure VI-11.

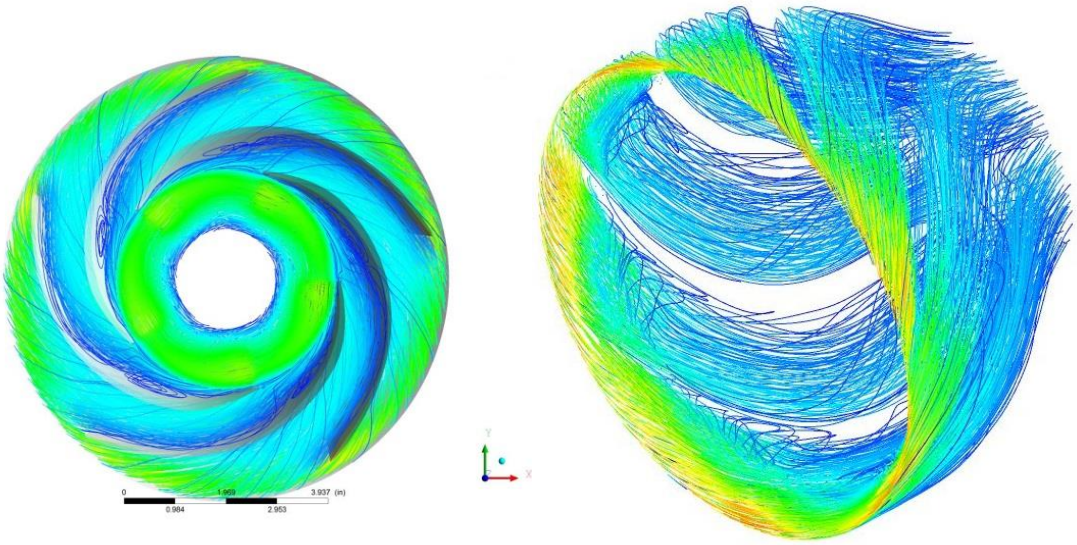

(a) (b)

Figure VI-13: Streamlines in the impeller (a) and diffuser (b) at a flow rate of 533 gpm for service with 200cP oil

Blade-to-blade views of the streamlines for rotational machinery are shown in Figure VI-14 Four different operating conditions were selected to study the influence of viscosity and flow rate. Figure VI-14(a) is the streamlines in case 1.2, representing low viscosity fluid at part-load flow rate. Figure VI-14(b) is the streamlines in case 1.7, representing low viscosity fluid at over-load flow rate. Figure VI-14(c) is the streamlines in case 5.1 representing high viscosity fluid at part-load flow rate. Figure VI-14(d) is the streamlines in case 5.6, representing high viscosity fluid at over-load flow rate. Blade-to-blade views of streamlines in the impeller are on the left of each figure, while in the diffuser are on the right.

In Figure VI-14(a), large recirculation zones occur along the blades in both the impeller and the diffuser. It shows that when pumping low viscosity fluid at part-load

flow rate, large recirculation spots will form along the blades in the impeller and the diffuser. For service with highly viscous fluid at part-load flow rate, the recirculation zones are still measurable as seen Figure VI-14(c). The comparison between case 1.1 and case 5.1 indicates that when pumping higher viscosity fluid at part-load flow rate, the recirculation zones will diminish in both size and quantity. In over-load flow rate conditions, no recirculation regions are observed for both water and highly viscous oil as shown in Figure VI-14(b) and Figure VI-14(d).

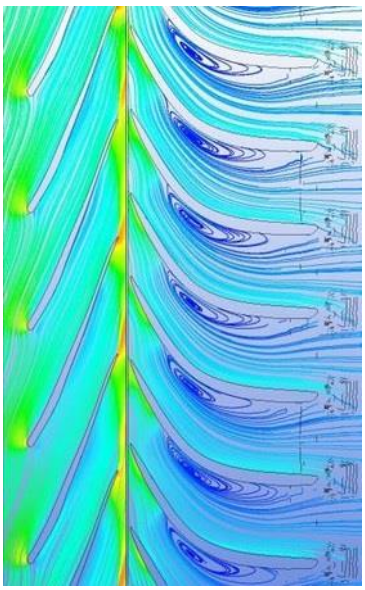

(a)

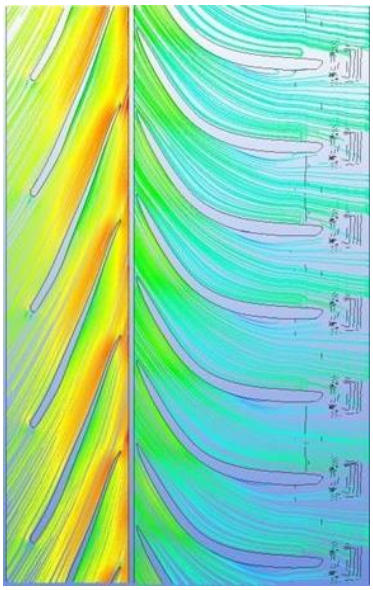

(b)

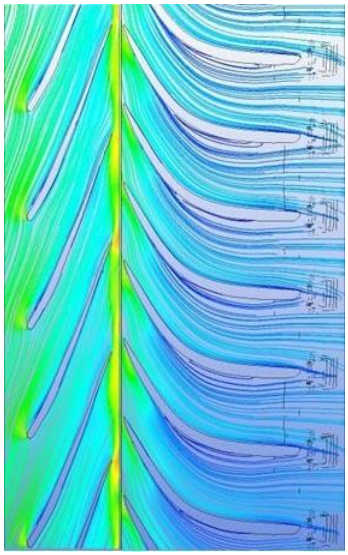

(c)

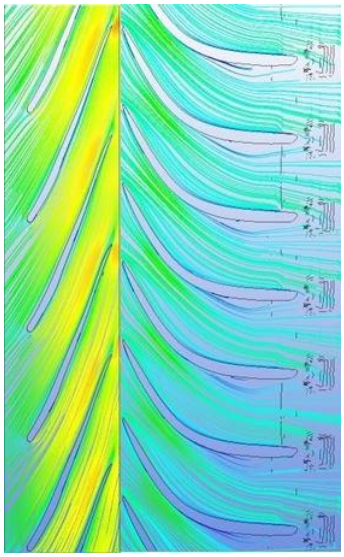

(d)

Figure VI-14: Blade-to-blade views of the streamlines in the impeller and diffuser in (a) Pumping water (1cP) at 583.3 gpm (b) Pumping water (1cP) at 1312 gpm (c) Pumping 200cP oil at 533.6 gpm (d) Pumping 200cP oil at 1423 gpm

VI.3. Performance Analysis

Figure VI-5 suggests that the pump performance heavily degraded when pumping highly viscous fluids. In high flow rate cases, the performance recession rate is even faster as the viscosity rise. According to the pump catalog in Figure IV-5, the pump stops working at a flow rate of 1750 gpm for service with pure water. This number decreases to around 1350 gpm when pumping 400cP oil at the same rotational speed based on Figure VI-5.

To better understand the influence of viscosity on the head performance of the pump, viscosity is taken as the variable for all the cases. Figure VI-15 shows the curves of pressure rises versus viscosities for groups of fluids at different flow rates. In this figure, in lower flow rate cases, the viscosity has less influence on the pressure rise. At a flow rate of 533 gpm, the performance drop in the pressure rise between 2.4cP oil case and 400cP oil case is merely 17.5%. By this trend, at the same flow rate, this pump is able to handle even much higher viscosity fluid with moderate head loss. However, in the over-load conditions, the pump performance degrades quickly when the viscosity of the fluid increases. At the flow rate of 1423 gpm, the head decays rapidly from 36psi for service with 2.4cP oil to -5psi for 400cP oil. The results indicate the viscosity of the fluids has more influence on the pump performance at higher flow rates.

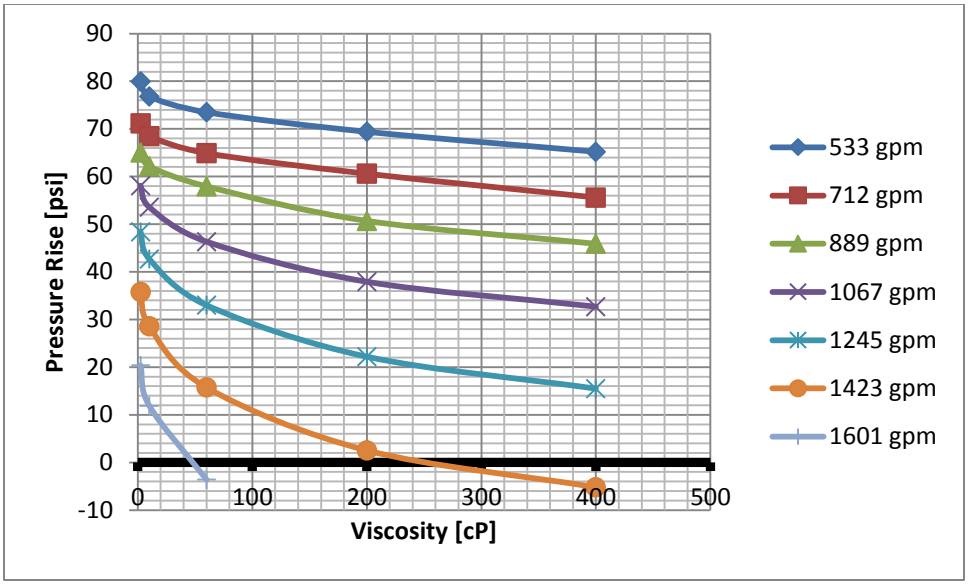

Figure VI-15: Pressure rises versus viscosities for different flow rates

A hydraulic efficiency analysis was performed to study the influence of viscosity on the pump efficiency and the best efficiency point. Eq. (VI-1) is the calculation for the pump efficiency

$$\eta = \frac{\rho g Q H}{T\omega} \tag{VI-1}$$

In the equation, ρ is the density of the fluid (kg/m3), g is the gravity (m/s2), Q is the flow rate (m3/s), H is the head (m), ω is the angular speed (rad/s) and T is the torque (N·m). $T\omega$ together is the shaft horsepower as shown in Figure VI-16. In the simulations, T is the torque provided by all the rotating surfaces in the hydraulic channels. It is calculated in the software Fluent by integrating the moment to the rotating axis of all moving internal walls.

Theoretically, the numerator in the equation is the product of pressure rise and flow rate, which represents the output power of the pump. The shaft power in the denominator may be treated as the input power from the shaft. Efficiency is then defined as the output power divided by the input power.

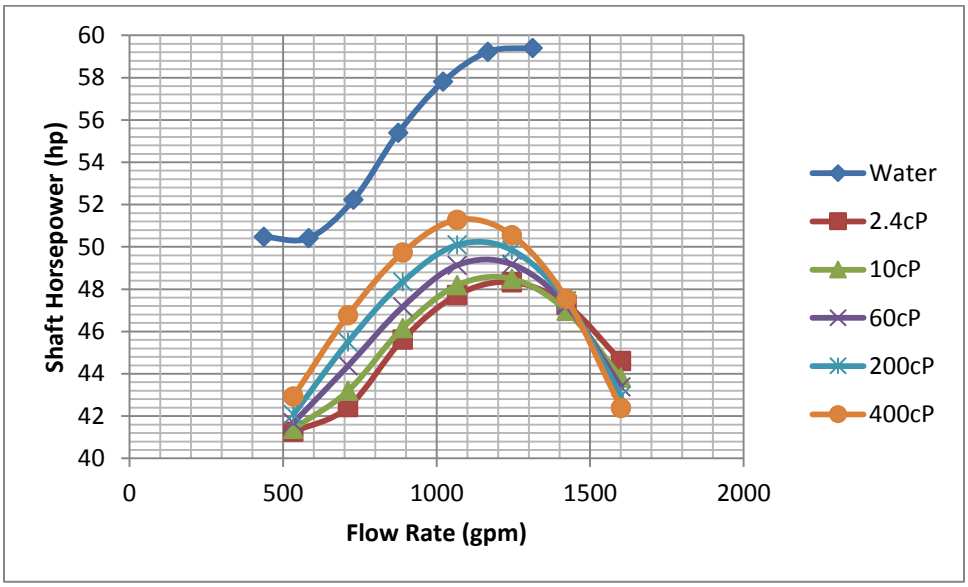

Figure VI-16: Shaft horsepower for all fluids

Figure VI-16 summarize the shaft horsepower in every case. At the same flow rate, the shaft power of the pump does not change considerably when pumping different viscosity fluids. It can be concluded that viscosity has slight influence on the shaft power of the pump. The curve for water is higher than all curves for service with oil. The difference is cause by the density difference between the oil and water. Thus the

efficiency of the pump is mainly decided by the density, flow rate and the product of hydraulic head and inlet flow rate in every case.

A comparison of the efficiency for service with pure water between the simulation results and the experimental results is posted in Figure VI-17. As expected, the efficiency in the simulation cases is higher than in experiment conditions. This is due internal leakage in the balance holes and the secondary flow paths causing, the efficiency curve of the experimental results to differ from the simulations and pump catalog in Figure IV-5. The best efficiency point is different than expected under the experiment conditions. And the fitting curve is not a smooth one as the curve from simulation results. Compared with the pump catalog, the efficiencies of simulation results are slightly higher. As discussed in part 1, the neglect of leakage and energy loss, the simplification of balance holes and the difference in the number of stages may be the reasons for the discrepancy of the curves. In simulation results, the best efficiency point is correct to be the same as the manufacture's suggestion and the shape of the efficiency curve from simulation results shows good consistency with the efficiency curve in the pump catalog in Figure IV-5.

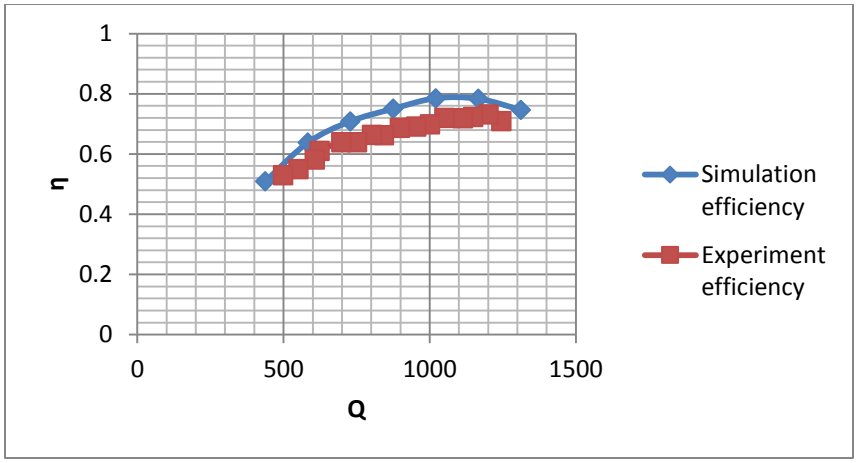

Figure VI-17: Comparison of the pump efficiencies between simulation results and experimental results for service with water

The efficiencies versus flow rates for water and all groups of oils are shown in Figure VI-18. In low flow rate cases, the pump efficiency degrades consistently due to the rise of viscosity. At a flow rate of 533.6 gpm, the deviation in efficiencies between 2.4cP oil case and 400cP oil case is 12%. However, at higher flow rates, the pump efficiency drops dramatically when the fluid viscosity rises. At the best efficiency point of pure water (1100 gpm), the pump efficiency in 2.4cP oil case is about 33% higher than the efficiency in 400cP oil case. The efficiency curve for water is not similar to all oil cases. So the influence of density on pump performance cannot be neglected.

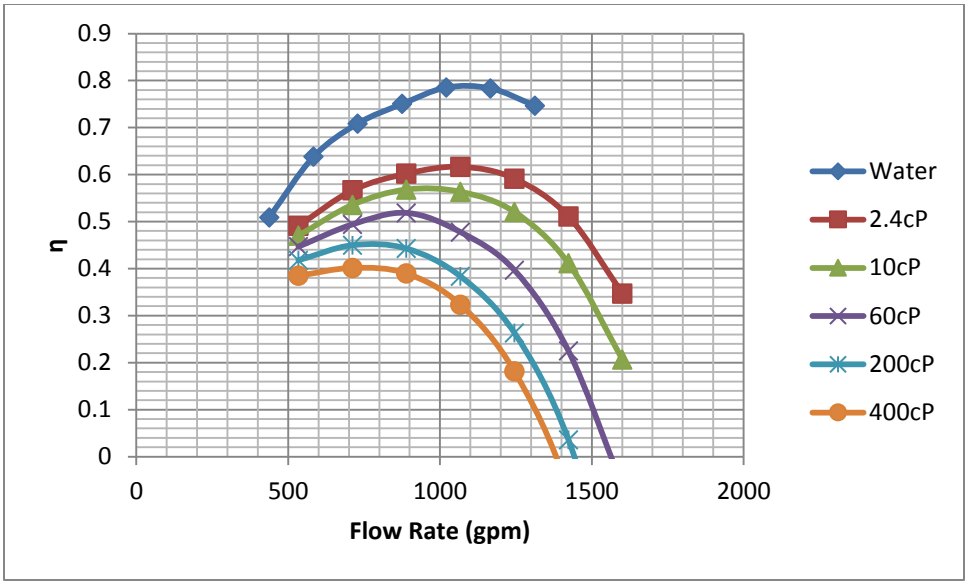

Figure VI-18: Pump efficiency curves for all fluids

Figure VI-18 proves the best efficiency points are different for various viscosity fluids at the same rotational speed. For service with pure water, the flow rate at the best efficiency point is 1100 gpm as shown in Figure IV-5. When pumping 400cP oil, the flow rate at the best efficiency point decreases to a little over 700 gpm. To better study the influence of viscosity on the pump efficiency, $Q_{BEP,V}/Q_{BEP}$ is used as a correction factor for the flow rate. In the factor, Q_{BEP} is the flow rate at the best efficiency point for service with pure water. $Q_{BEP,V}$ is the flow rate at the best efficiency point for service with any fluid in this study. Since the oil and water in this study have different densities, kinematic viscosity is employed to be the independent variable in this analysis. Figure VI-19 shows the $Q_{BEP,V}/Q_{BEP}$ as a function of the kinematic viscosity for all fluids. The X-axis is the modification of kinematic viscosity for all fluids.

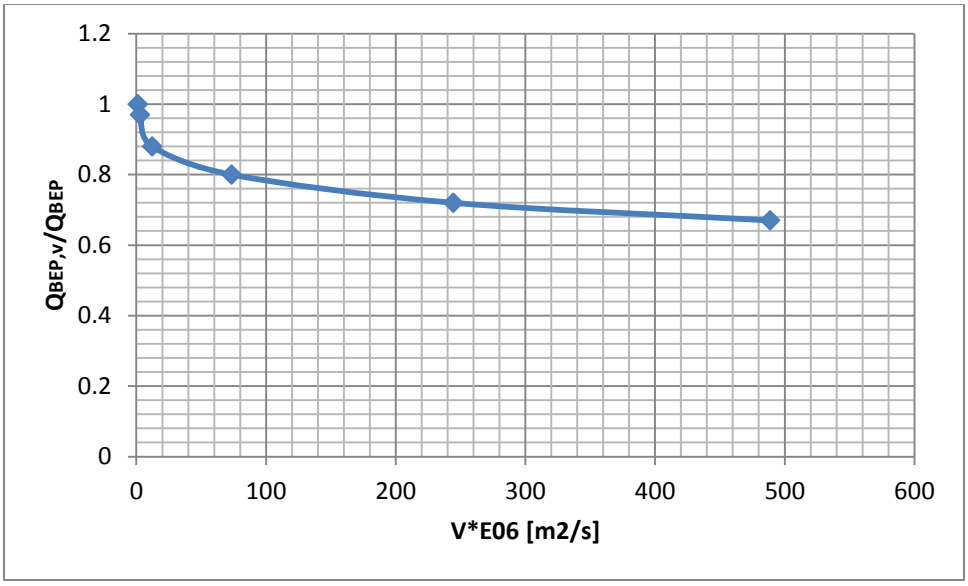

Figure VI-19: $Q_{BEP,V}/Q_{BEP}$ versus kinematic viscosity for all fluids

This figure clearly demonstrates the change in best efficiency point when pumping highly viscous oil. By adopting kinematic viscosity, this curve may be used to predict the best efficiency point for transporting any other fluids. When the kinematic viscosity of fluid rises, the flow rate has to be lowered to achieve the best efficiency for the pump. In an ESP, the number of stages has to be added to reach the same head; meanwhile the production rate of the pump is declining.

Gülich [6],[7] thought the ratio $Q_{BEP,V}/Q_{BEP}$ is the actual correction factor for the flow rate. For all the pumps he investigated, the correction factor is still applicable for points other than the best efficiency point.

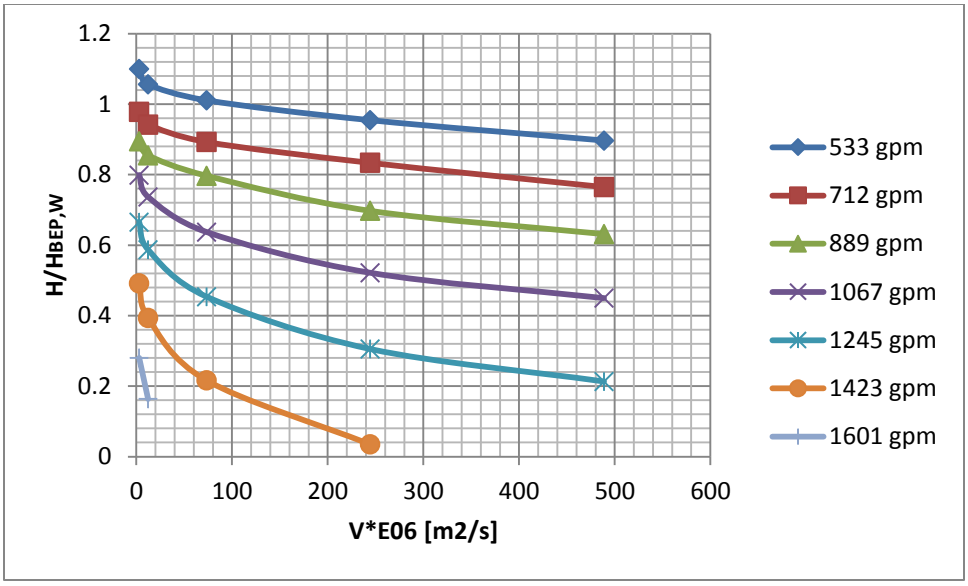

Figure VI-20: $H/H_{BEP,w}$ versus kinematic viscosity for all fluids

A correction factor for the head is studied by the same method as the flow rate in Figure VI-20. The hydraulic head is normalized by dividing the head for service with pure water at the best efficiency point in every case. Compared with Figure VI-15, this chart reveals the influence of viscosity on the pump performance more objectively. The employment of kinematic viscosity enables the cases for service with pure water to be added in the figure. For high flow rate cases, the head recession curve is steeper than low flow rate cases. At a half-load flow rate (533 gpm), the pump performance drops moderately with the rise in viscosity. This stage of ESP can still provide large percentage of the original hydraulic head when the viscosity of fluid rises from 1cP to 400cP. However, at a flow rate of 1423 gpm, the pump performance is quickly degraded when the viscosity of fluid increases. The curves prove that at higher flow rates, the pump performance is more sensitive to the viscosity of fluids.

VI.4. Dimensionless Analysis

A dimensionless analysis was performed by Timar [8] to seek a flow similarity law for centrifugal pumps working at different rotational speeds. In the same way, this research used the dimensionless numbers to understand the influence of viscosity on ESP performance. For the sake of convenience, some of the dimensionless numbers are modified based on Timar's work. They are calculated by the following equations.

$$\Psi = \frac{\Delta P}{\rho {D_s}^2 \omega^2} \tag{VI-2}$$

$$\Phi = \frac{Q}{\omega {D_s}^3} \tag{VI-3}$$

$$Re_w = \frac{\rho \omega {D_s}^2}{\mu} \tag{VI-4}$$

Eq. (VI-2) is the calculation for head coefficient Ψ. Eq. (VI-3) is the definition of flow rate coefficient Φ; and Eq. (VI-4) represents the rotating Reynolds number Re_w. In all equations, ΔP is the pressure rise of the pump (pascal), Q is the flow rate of the stage (m^3/s), ρ is the density of the fluid (kg/m^3), ω means the angular speed of the impeller (rad/s), μ is the dynamics viscosity of the fluid (kg/ms), D_s is defined as a length scale of the pump geometries. In this model, D_s is the impeller outlet mean diameter which is 200.8 mm.

Table VI-1: Rotating Reynolds number for all fluids

Fluids	2.4cP	10cP	60cP	200cP	400cP	Water
Re_w	5139552	1233492	205582.1	61674.62	30837.31	15044870

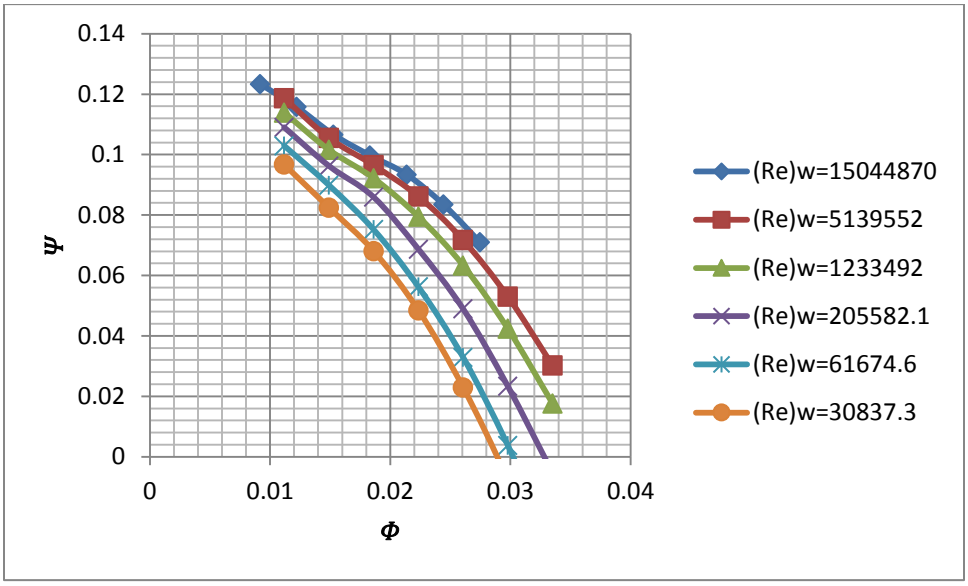

Figure VI-21: Head coefficient versus flow rate coefficient for all fluids

Table VI-1 summarizes the rotating Reynolds numbers for all testing fluids. Figure VI-21 is the head coefficient for every group of fluids as a function of flow rate coefficient. In Figure VI-5, the curves indicate that large head degradation occurs when pumping highly viscous oil. Similarly, this figure suggests head coefficient is lowered when rotating Reynolds number is decreased or flow rate coefficient is increased. Solano [20] concluded that head coefficient Ψ should be a function of flow rate coefficient Φ and rotating Reynolds number Re_w for ESPs.

As expected, the curves in Figure VI-21 are similar with the ones in Figure VI-5. The benefit to employ these dimensionless numbers is providing a systematic and mathematic understanding of how pump performance degrades. All the fluid properties and units have been taken into consideration by nondimensionalization. And similarity laws can be easily established on the same or similar pump geometries for future researches working at variable rotational speeds.

A pump efficiency analysis was performed by using dimensionless numbers in Figure VI-22. This is the same efficiency from Figure VI-18 but now presented as a function of the flow rate coefficient.

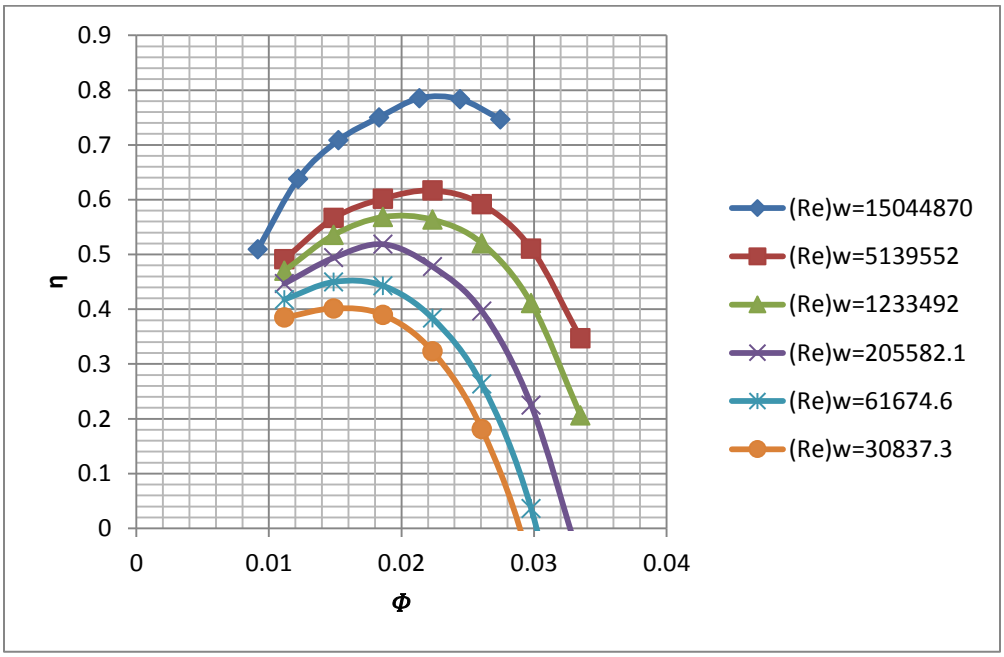

Figure VI-22: Pump efficiency versus flow rate coefficient for all fluids

For every curve in Figure VI-22, a multi order polynomial trend line is added to offer a rough estimation of the performance curves of the pump for service with different viscosity fluids as shown in Figure VI-23.The starting points of all curves are close to the origin. For fluids with higher rotating Reynolds number, the flow rate coefficient at the best efficiency point tends to be larger. The maximum efficiency is lower when pumping fluids with lower rotating Reynolds number. Based on the figure, the pump efficiency can be represented as a function of flow rate coefficient Φ and the rotating Reynolds number Re_w.

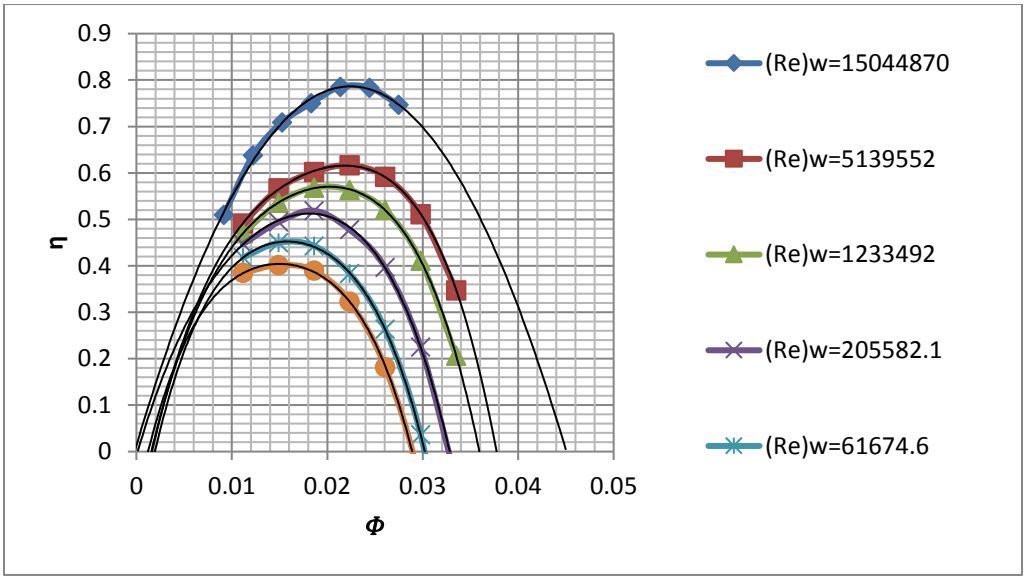

Figure VI-23: Pump efficiency versus flow rate coefficient with trend lines

As stated above, head coefficient in every case can be expressed as a function of flow rate coefficient and rotating Reynolds number. Figure VI-24, created by the

software TableCurve 3D, plots the points of the three dimensionless numbers for all cases. The X-axis is flow rate coefficient Φ, Y-axis is the common logarithm (logarithm to base 10) of rotating Reynolds number Re_w and Z-axis represents the head coefficient Ψ. The fitting curved surface, calculated by simple equations, provides a clear view of the relationship among the three dimensionless numbers for this research. Since all the points are included, this curved surface may be regarded as a universal equation to calculate the pump performance. For one stage of this pump, head coefficient under any working conditions can be determined from the rotating Reynolds number and flow rate coefficient. Thus, the surface can be used to predict the hydraulic head for service with any other known fluids with various inlet flow rates. Moreover, affinity laws can be applied to determine the hydraulic head for cases under different rotational speeds or in similar pump geometries.

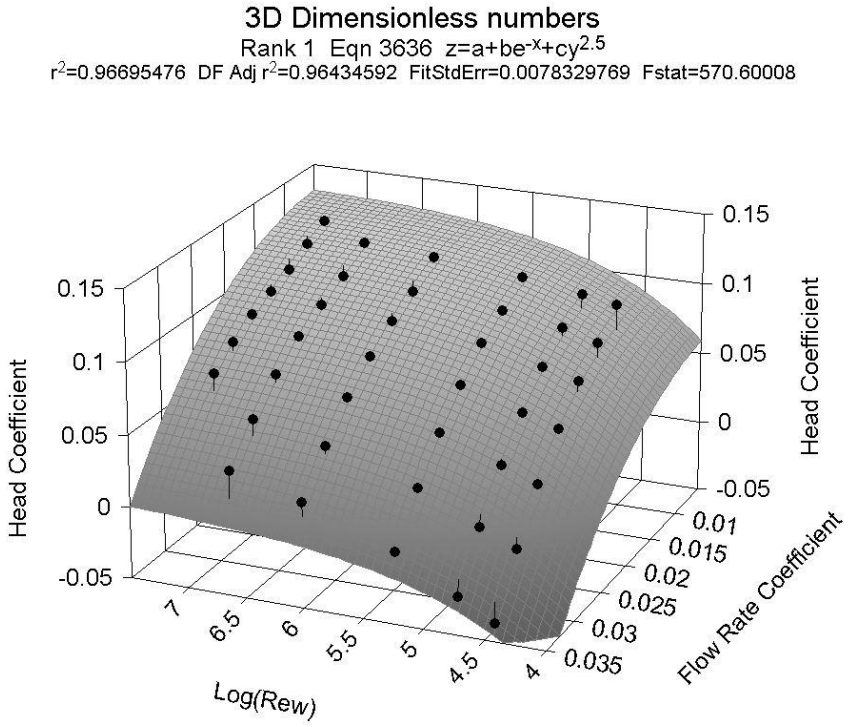

Figure VI-24: Head coefficient versus common logarithm of rotating Reynolds number and flow rate coefficient in TableCurve 3D

A simpler way to acquire a universal solution is to modify the dimensionless numbers in a 2D chart. Figure VI-25 provides an empirical universal pump performance curve. The independent variable is set as $\Phi * Re_w$^-0.066, which is purely an empirical estimation with no physical meanings. It combines the influence of flow rate coefficient and Reynolds number. The Y-axis is set as head coefficient. In this figure, the curves of all groups of cases overlap and approach a universal curve. The new formed curve can be used as an empirical method to predict the pump performance under different working conditions.

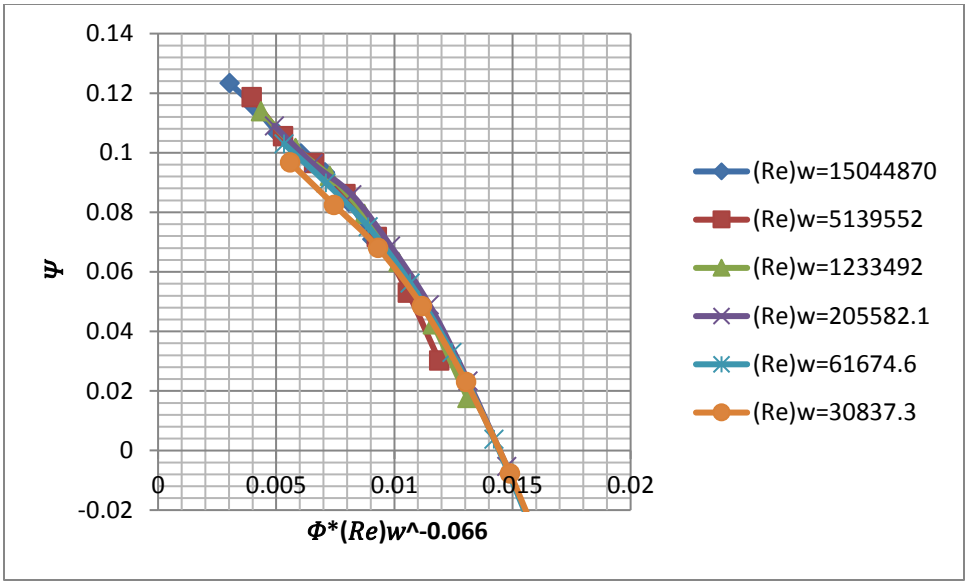

Figure VI-25: Empirical pump performance curve by modified dimensionless numbers

Parameters related to power of the stage are also of importance to the pump performance. The following equations are the nondimensionlization of shaft power, output power and drag power.

$$N_{sh} = \frac{P_{sh}}{\rho {D_s}^5 \omega^3} \tag{VI-5}$$

$$N_{out} = \frac{QH}{\rho {D_s}^5 \omega^3} \tag{VI-6}$$

$$N_{drag} = \frac{P_{drag}}{\rho {D_s}^5 \omega^3} \tag{VI-7}$$

Eq. (VI-5) is the calculation for shaft power coefficient N_{sh}. Eq. (VI-6) is the definition of output power coefficient N_{out}; and Eq. (VI-7) represents the drag power coefficientN_{drag}. In all equations, H is the head of the pump (m), Q is the flow rate of

the stage (m^3/s), ρ is the density of the fluid (kg/m^3), ω means the angular speed of the impeller (rad/s), D_s is defined as a length scale of the pump geometries. P_{sh} is the shaft power of the pump and P_{drag} is the drag power of the stage.

The shaft power coefficient N_{sh}, which represents the power from shaft to the pump, is an important parameter for pump users. Figure VI-26 is the shaft power coefficient N_{Sh} versus flow rate coefficient for all cases. The Y-axis has been adjusted to magnify the difference of the curves. Compared to Figure VI-16, Figure VI-26 is able to include the curve for water regardless of the difference in density. When the flow rate coefficient is less than 0.3, the shaft power coefficient is higher in lower Reynolds number cases. This indicates that under a certain flow rate, the shaft provides more power for service with higher viscous fluids. When the flow rate coefficient is over 0.3, shaft power coefficient is lower in lower Reynolds number cases. This may be caused by the fall in pressure rise when pumping highly viscous fluids at high flow rate.

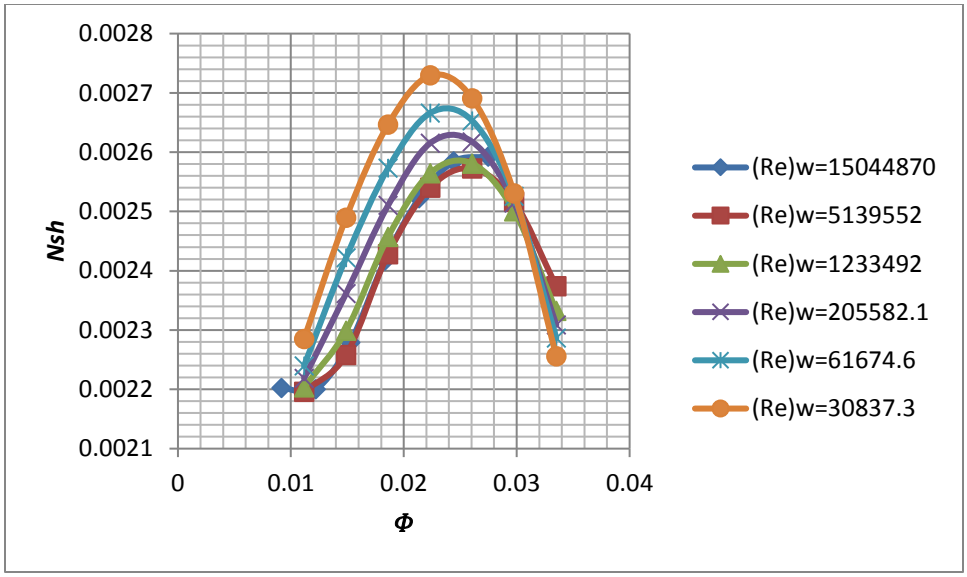

Figure VI-26: Shaft power coefficient versus flow rate coefficient for all fluids

Figure VI-27 is the output power versus flow rate coefficient for every case. In fact, the output power coefficient, also called hydraulic power, is calculated as the product of head coefficient and flow rate coefficient. It represents the actual power absorbed by the output fluid. The curves in Figure VI-27 are identical to the efficiency curves. For every fluid, there is a maximum output power point which is a function by the flow rate coefficient and the rotating Reynolds number. Then for service with every fluid, the pump has a highest output power.

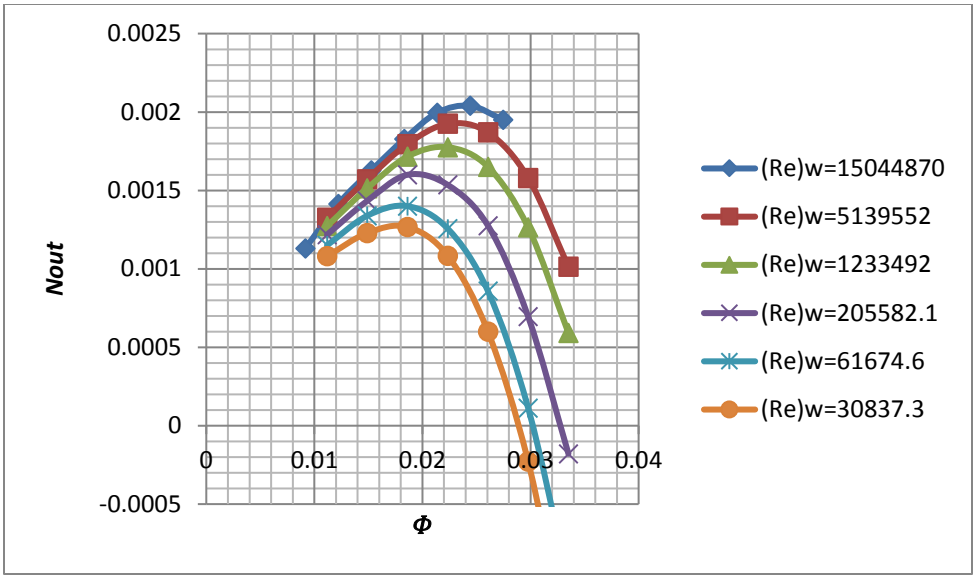

Figure VI-27: Output power coefficient versus flow rate coefficient for all fluids

Figure VI-28 is drag power coefficient versus flow rate coefficient in every case. Drag power is the power dissipated in the fluid. It can also be regarded as the wasted power. The calculation of drag power coefficient is shaft power coefficient minus output power coefficient. The drag power coefficient for the fluid which has lower rotating Reynolds number is higher than the fluid which has higher Reynolds number. This trend indicates that more power is dissipated when pumping more viscous fluid under the same working condition. Like the output power coefficient curves, the curves in Figure VI-28 have a lowest point. The points can be chosen as the best working conditions to minimize the drag power and enhance the efficiency.

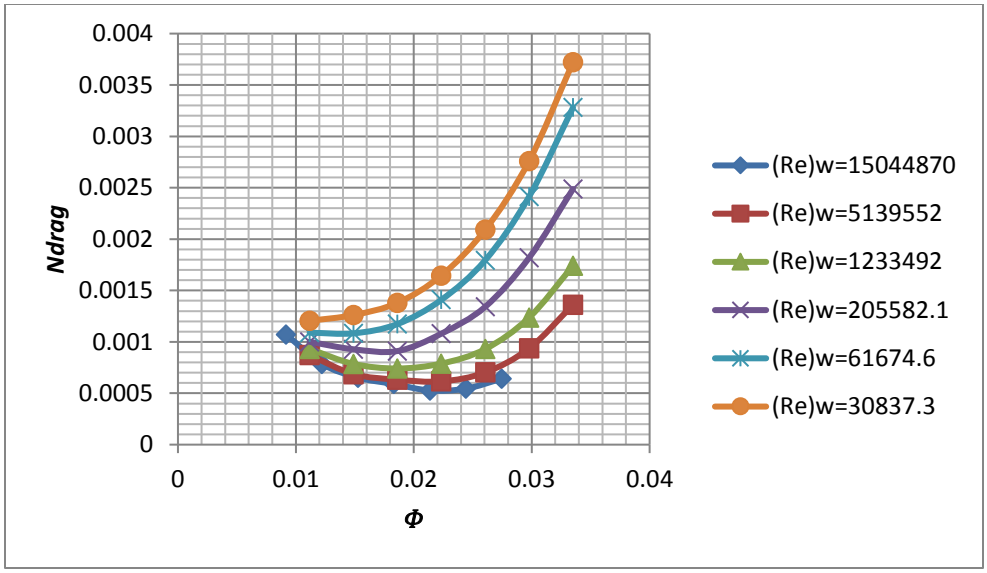

Figure VI-28: Drag power coefficient versus flow rate coefficient for all fluids

Figure VI-29**:** Output power coefficient versus head coefficient and flow rate coefficient in TableCurve 3D is the output power coefficient versus head coefficient and flow rate coefficient. Figure VI-30 is the drag power coefficient versus head coefficient and flow rate coefficient. The curved surface of the plots is a smooth surface and fitted by simple functions.

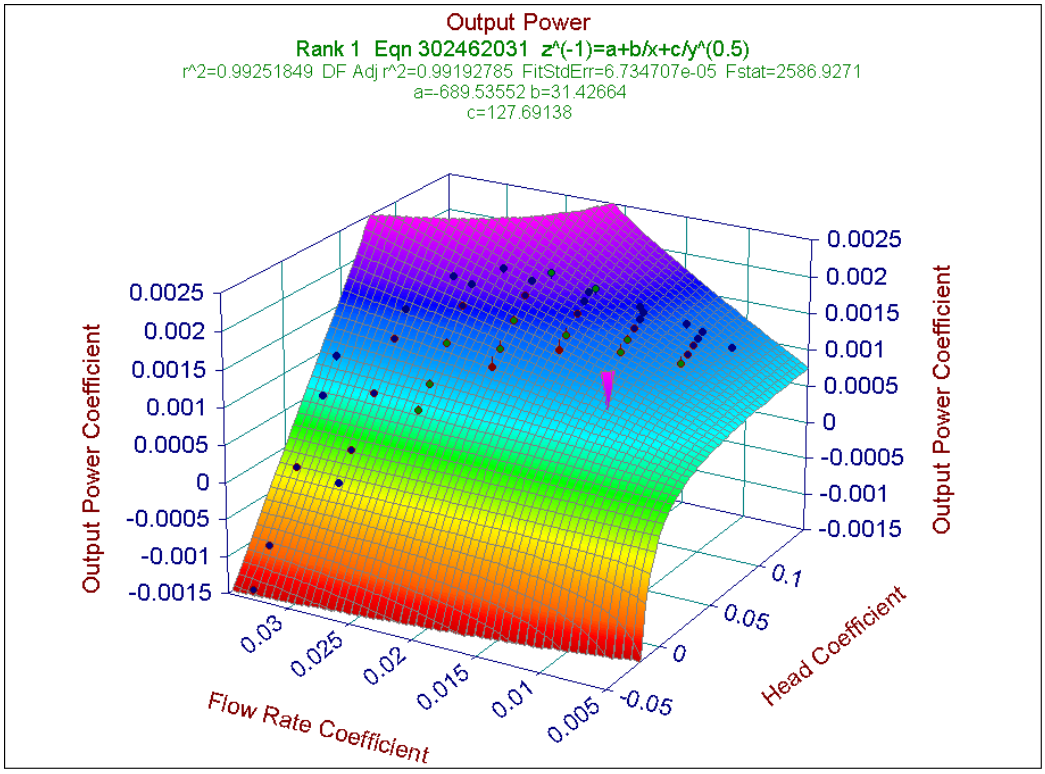

Figure VI-29: Output power coefficient versus head coefficient and flow rate coefficient in TableCurve 3D

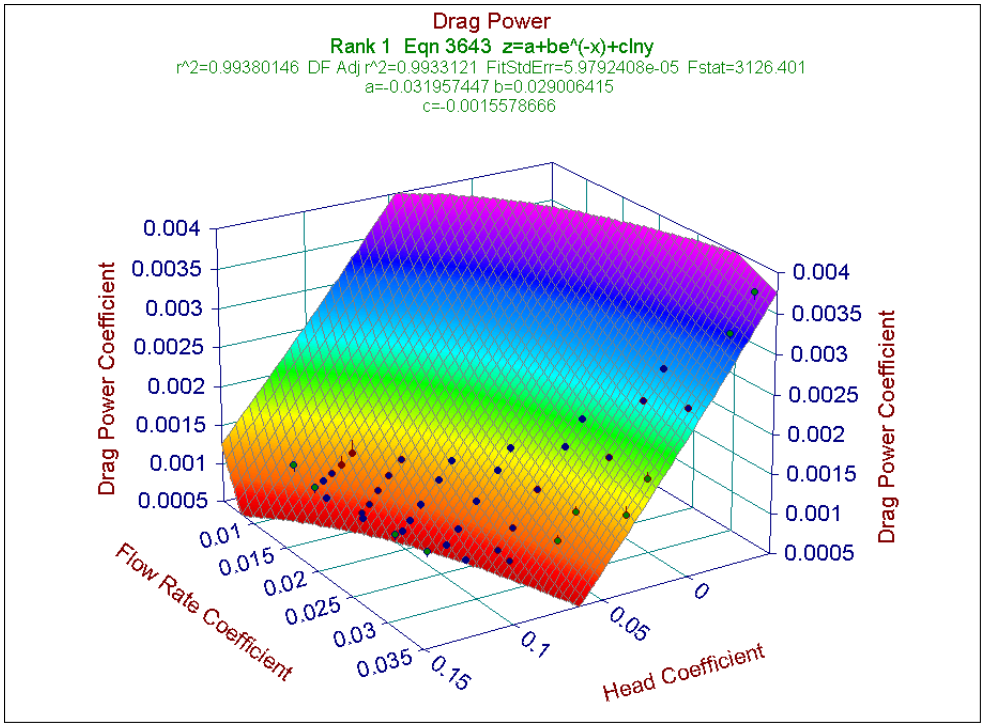

Figure VI-30: Drag power coefficient versus head coefficient and flow rate coefficient in TableCurve 3D

For every set of known flow rate coefficient Φ and rotating Reynolds number Re_w, the head coefficient Ψ can be obtained from Figure VI-24. As stated above, the output power coefficient N_{out} is the product of Φ and Ψ. The drag power coefficient N_{drag} may be obtained from Figure VI-30. Then the shaft power coefficient N_{sh} can be calculated as N_{out}+N_{drag}. So under every condition, all three power coefficients can be calculated from Figure VI-24 and Figure VI-30.

All the dimensionless numbers are meaningful for pump users. The dimensionless numbers provide a systematic and mathematic relation of the pump performance.

VII. CONCLUSIONS

In this research, a CFD method was adopted to investigate the flow behavior and pressure performance of one stage of an Electrical Submersible Pump. The influence of viscosity on the pump performance was studied throughout the analysis.

Compared with the pump catalog and experimental results, the simulation results show good consistency and validate the model of the pump. Head degradation due to the use of high viscosity fluids is clearly illustrated by plotting the pressure rise of the pump in every case. Pressure change in the impeller and the diffuser are studied separately. It was revealed that when pumping highly viscous fluids at high flow rate, the diffuser can cause pressure lose rather than provide positive hydraulic head.

Four different cases were chosen to investigate the flow behavior inside the pump channels. For low viscosity fluid in part-load conditions, large recirculation regions are observed along the blades in the impeller and the diffuser. When pumping high viscosity fluid at the same part-load flow rate, recirculation regions decrease in both quantity and size. For over-load flow rate conditions, no recirculation zones are found for both low viscosity fluid and high viscosity fluid.

It is proven that the pump performance is more sensitive to the rise of viscosity at higher flow rates than lower flow rates. In this research, an analysis of the pump efficiency is performed. The maximum efficiency is lowered for service with higher viscosity fluid. Moreover, the flow rate at the best efficiency point is descending as the viscosity of fluid increases. Thus, to keep the pump working at the best efficiency point

for service with higher viscosity fluids, flow rate (which is also the production rate) needs to be decreased, while the number of stages must be added in order to maintain the hydraulic head of the whole pump.

Dimensionless numbers are introduced to better understand the influence of viscosity on pump performance. It is concluded that head coefficient and the pump efficiency can be represented as functions of flow rate coefficient and rotating Reynolds number. A 3D curved surface is calculated based on all cases as a universal solution. The surface can be used to predict the pump performance under various working conditions.

Power coefficients are discussed. Output power coefficient is directly obtained from head coefficient and flow rate coefficient. The drag power coefficient which is caused by viscosity proved to be a function of head coefficient and flow rate coefficient. Then the shaft power coefficient can be obtained from these two power coefficients.

For the future work, the recommendation is to investigate the pump performance at different rotational speeds. As the dimensionless numbers are adopted, affinity laws can be used to predict the pump performance at various rotational speeds.

REFERENCES

[1] Schlumberger. "*Pushing Up the Range of Options*." 2015; Available from: http://www.slb.com/~/media/Files/artificial_lift/industry_articles/201503-upstream-tech-pushing-up-range-of-options.pdf.

[2] Baker Hughes. "*ESP System Technology Overview*." 2013.

[3] ESDU, *Radial mixed and axial flow pumps. Introduction*. ESDU Series on Fluid Mechanics. 1980: ESDU. 61.

[4] Karassik, I.J. and J.T. McGuire, *Centrifugal pumps. 2nd ed*. 1998: New York : Chapman & Hall : International Thomson, 1998 2nd ed.

[5] Ippen, A. T., 1945, "*The influence of viscosity on centrifugal pump performance*," Issue 199 of Fritz Engineering Laboratory report, ASME Paper No. A-45-57

[6] Gülich, J.f., 1999, "*Pumping Highly Viscous Fluids with Centrifugal Pumps — Part 1*." World Pumps 1999(395): p. 30-34.

[7] Gülich, J.f., 1999, "*Pumping Highly Viscous Fluids with Centrifugal Pumps — Part 2."* World Pumps 1999(396): p. 39-42.

[8] Timar, P., "*Dimensionless Characteristics of Centrifugal Pump."* Chemical Papers- Slovak Academy of Sciences, 2005. 59: p. 500-503.

[9] Feng, J., F.K. Benra, and H. Dohmen, "*Application of Different Turbulence Models in Unsteady Flow Simulations of a Radial Diffuser Pump."* Anwendung verschiedener Turbulenzmodelle zur Simulation der transienten Strömung in einer Radialpumpe mit beschaufeltem Diffusor. 2010. 74(3): p. 123.

[10] Majidi, K. and H.E. Siekmann, "*Numerical Calculation of Secondary Flow in Pump Volute and Circular Casings using 3D Viscous Flow Techniques."* International Journal of Rotating Machinery, 2000. 6(4): p. 245.

[11] Barrios, L.J., "*Visualization and Modeling of Multiphase Performance inside an Electrical Submersible Pump"*. 2007: (PHD Thesis, The University of Tulsa).

[12] Rasmy Marsis, E.G. and G. Morrison, "*CFD Simulation and Experimental Testing of Multiphase Flow Inside the MVP Electrical Submersible Pump"*. 2013: (PHD Thesis, Texas A & M University).

[13] Stel, H., Sirino T., P.R.Pamella., "*CFD Investigation of the Effect of Viscosity on a Three-Stage Electric Submersible Pump*." In *ASME 2014 4th Joint US-European Fluids Engineering Division Summer Meeting collocated with the ASME 2014 12th International Conference on Nanochannels, Microchannels, and Minichannels*. 2014. American Society of Mechanical Engineers.

[14] Sirino T., Stel,H., "*Numerical study of the influence of viscosity on the performance of an Electric Submersible Pump".* In *ASME 2013 Fluids Engineering Division Summer Meeting* 2013. American Society of Mechanical Engineers.

[15] Carvajal Diaz, N.I. and G. Morrison, "*Effects of Sand on the Components and Performance of Electric Submersible Pumps*." 2013: (MS Thesis, Texas A & M University).

[16] Sun, D. and M.G. Prado, "*Single-Phase Model for Electric Submersible Pump (ESP) Head Performance"*. SPE Journal, 2006. 11(01): p. 80-88.

[17] Fluent, A., *Ansys Fluent theory guide.* ANSYS Inc., USA, 2011.

[18] Calumet Speciaty Products Parteners, L.P. "*Conosol Products*." 2008; Available from:http://www.calumetsolvents.com/images/spec-sheets/Oil_Drilling_Conosols_2-12.pdf.

[19] Sujan Reddy and G. Morrison, "*Experimental Results of an Electric Submersible Pump WJE-1000"*. 2016, Texas A & M University.

[20] Solano, E.A., "*Viscous Effects on the Performance of Electro Submersible Pumps (ESP's)"*. 2009: (MS Thesis, The University of Tulsa).

APPENDIX A

Table A-1: Pressure rise for three stages for service with water from experimental results

Liquid Flow Rate	Pressure Rise(psi)	Liquid Flow Rate	Pressure Rise(psi)
1245.454492	150.9168723	843.9751672	210.585432
1201.899912	164.726172	802.76351	215.3792913
1149.460445	171.8517462	751.5724593	220.9897089
1113.994854	179.2126045	698.2985364	227.1165952
1050.350146	187.6568339	623.8918205	236.0475731
1001.08742	194.3274047	607.1648746	238.1256344
954.0869712	198.1714808	551.470833	245.3765626

Table A-2: Pressure difference for the stage for all oils in psi

Flow Rate	2.4cP	10cP	60cP	200cP	400cP
533.6437114	79.98	77.52	73.748122	69.39	65.05
711.5146182	71.13	68.67	65.19088	61.13	55.76
889.2677584	65.05	62.14	57.93898	50.83	43.87
1067.271927	58.08	53.39	46.33594	37.92	29.37
1245.150582	48.37	42.42	32.702368	21.82	11.38
1423.029236	35.75	28.35	15.732922	2.53	-10.373918
1600.907891	20.37	11.53	-4.42736	-20.526578	-35.755568

Table A-3: Pump efficiency for all fluids

Case Series	2.4cP	10cP	60cP	200cP	400cP	Water
Case 1	0.491194	0.474428	0.448228	0.417825	0.383837	0.50923
Case 2	0.566434	0.53705	0.496285	0.453776	0.402733	0.637925
Case 3	0.601953	0.568313	0.518634	0.443918	0.372463	0.708707
Case 4	0.616629	0.563492	0.477827	0.383619	0.290173	0.750268
Case 5	0.591571	0.517148	0.393095	0.258817	0.13309	0.785291
Case 6	0.510863	0.407753	0.225005	0.036084		0.783426
Case 7	0.3472	0.199945				0.746831

Table A-4: Shaft horsepower in all cases in hp

Case	2.4cP	10cP	60cP	200cP	400cP	Water
Case 1	41.25464	41.39586	41.6841	42.07892	42.93298	50.47283
Case 2	42.42283	43.19307	44.37177	45.50537	46.77169	50.41746
Case 3	45.62008	46.16558	47.16389	48.34317	49.72644	52.2267
Case 4	47.72817	48.18595	49.13484	50.09016	51.27873	55.38859
Case 5	48.33105	48.48901	49.178	49.84721	50.55373	57.80759
Case 6	47.27485	46.97373	47.23869	47.45202	47.5425	59.21902
Case 7	44.59979	43.81598	43.37746	42.96328	42.37737	59.40609

Table A-5: Pressure drop in the inlet for all oils in psi

Flow Rate	2.4cP	10cP	60cP	200cP	400cP
533.6437114	0.72519	0.580152	0.72519	0.870228	1.160304
711.5146182	1.015266	2.17557	1.305342	1.45038	1.595418
889.2677584	1.305342	1.305342	0.870228	2.030532	2.320608
1067.271927	1.740456	2.030532	2.320608	2.755722	3.045798
1245.150582	2.17557	2.610684	2.90076	3.62595	4.061064
1423.029236	2.755722	3.190836	3.770988	4.496178	5.221368
1600.907891	3.480912	4.061064	4.786254	5.511444	6.381672

Table A-6: Pressure rise in the impeller for all oils in psi

Flow Rate	2.4 cP	10cP	60cP	200cP	400cP
533.6437114	63.96176	62.65642	61.061	59.03047	56.8549
711.5146182	61.061	60.91596	57.87016	55.54955	52.79383
889.2677584	58.59535	56.56482	53.8091	50.32819	46.41216
1067.271927	54.53429	51.63353	47.86254	43.65644	38.87018
1245.150582	49.31292	45.68697	40.61064	35.53431	29.87783
1423.029236	43.22132	37.99996	32.0534	25.9618	19.29005
1600.907891	36.2595	30.1679	22.33585	14.64884	6.961824

Table A-7: Pressure change in the diffuser for all oils in psi

Flow Rate	2.4 cP	10cP	60cP	200cP	400cP
533.6437114	16.74819	15.44285	13.41231	11.23674	9.35125
711.5146182	11.09171	9.931402	8.62606	7.030642	4.564996
889.2677584	7.755832	6.885604	5.00011	2.534464	-0.22126
1067.271927	5.290186	3.984844	0.794008	-2.97698	-6.45789
1245.150582	1.229122	-0.65637	-5.00751	-10.0838	-14.435
1423.029236	-4.71744	-6.45789	-12.5495	-18.9312	-24.4426
1600.907891	-12.4045	-14.58	-21.977	-29.664	-36.3357

Table A-8: Kinematic viscosity in all cases

*V**E06	2.4cP	10cP	60cP	200cP	400cP	Water
Case 1	2.932551	12.21896	73.31378	244.3793	488.7586	1.001803
Case 2	2.932551	12.21896	73.31378	244.3793	488.7586	1.001803
Case 3	2.932551	12.21896	73.31378	244.3793	488.7586	1.001803
Case 4	2.932551	12.21896	73.31378	244.3793	488.7586	1.001803
Case 5	2.932551	12.21896	73.31378	244.3793	488.7586	1.001803
Case 6	2.932551	12.21896	73.31378	244.3793	488.7586	1.001803
Case 7	2.932551	12.21896	73.31378	244.3793	488.7586	1.001803

Table A-9: Head correction factor in all cases

H/H_{BEP}	2.4cP	10cP	60cP	200cP	400cP	Water
Case 1	1.099987	1.066078	1.014218	0.954379	0.89454	1.395192
Case 2	0.978314	0.944406	0.896535	0.840685	0.766884	1.309423
Case 3	0.89454	0.854647	0.796803	0.699066	0.603324	1.205702
Case 4	0.798798	0.736964	0.637233	0.521545	0.403861	1.127912
Case 5	0.665158	0.583378	0.449738	0.300141	0.156527	1.056105
Case 6	0.491625	0.389899	0.216366	0.034855	-0.14267	0.944406
Case 7	0.280194	0.158522	-0.06089	-0.28229	-0.49173	0.802787

Table A-10: Dimensionless number Ψ in all cases

Ψ	2.4cP	10cP	60cP	200cP	400cP	Water
Case 1	0.118653	0.114995	0.109401	0.102947	0.096492	0.123388
Case 2	0.105529	0.101871	0.096707	0.090683	0.082722	0.115803
Case 3	0.096492	0.092189	0.085949	0.075407	0.065079	0.10663
Case 4	0.086165	0.079495	0.068737	0.056258	0.043564	0.09975
Case 5	0.071749	0.062928	0.048512	0.032375	0.016884	0.0934
Case 6	0.05303	0.042058	0.023339	0.00376	-0.01539	0.083521
Case 7	0.030224	0.017099	-0.00657	-0.03045	-0.05304	0.070997

Table A-11: Dimensionless number Φ in all case

Φ	2.4cP	10cP	60cP	200cP	400cP	Water
Case 1	0.011169	0.011169	0.011169	0.011169	0.011169	0.009157
Case 2	0.014892	0.014892	0.014892	0.014892	0.014892	0.012209
Case 3	0.018612	0.018612	0.018612	0.018612	0.018612	0.01526
Case 4	0.022338	0.022338	0.022338	0.022338	0.022338	0.018314
Case 5	0.026061	0.026061	0.026061	0.026061	0.026061	0.021366
Case 6	0.029783	0.029783	0.029783	0.029783	0.029783	0.024419
Case 7	0.033506	0.033506	0.033506	0.033506	0.033506	0.027471

Table A-12: Dimensionless number N_{sh} in all cases

N_{sh}	2.4cP	10cP	60cP	200cP	400cP	Water
Case 1	0.002197	0.002204	0.00222	0.002241	0.002286	0.002203
Case 2	0.002259	0.0023	0.002363	0.002423	0.00249	0.002201
Case 3	0.002429	0.002458	0.002511	0.002574	0.002648	0.00228
Case 4	0.002541	0.002566	0.002616	0.002667	0.00273	0.002418
Case 5	0.002573	0.002582	0.002619	0.002654	0.002692	0.002524
Case 6	0.002517	0.002501	0.002515	0.002527	0.002531	0.002585
Case 7	0.002375	0.002333	0.00231	0.002288	0.002256	0.002593

Table A-13: Dimensionless number N_{out} in all cases

N_{out}	2.4cP	10cP	60cP	200cP	400cP	Water
Case 1	0.001325	0.001272	0.001218	0.00115	0.00108	0.00113
Case 2	0.001572	0.001513	0.001434	0.001339	0.001228	0.001414
Case 3	0.001796	0.001716	0.0016	0.0014	0.001267	0.001627
Case 4	0.001925	0.001776	0.001535	0.001257	0.001084	0.001827
Case 5	0.00187	0.001651	0.001276	0.000858	0.000599	0.001996
Case 6	0.001579	0.001264	0.000695	0.000112	-0.00023	0.002039
Case 7	0.001013	0.000591	-0.00018	-0.00099	-0.00147	0.00195

Table A-14: Dimensionless number N_{drag} in all cases

N_{drag}	2.4cP	10cP	60cP	200cP	400cP	Water
Case 1	0.000871	0.000931	0.001001	0.00109	0.001205	0.001073
Case 2	0.000686	0.000786	0.000928	0.001083	0.001261	0.000786
Case 3	0.000632	0.000741	0.000911	0.001173	0.001379	0.000652
Case 4	0.000616	0.000789	0.00108	0.001409	0.001646	0.00059
Case 5	0.000703	0.00093	0.001342	0.001795	0.002092	0.000527
Case 6	0.000937	0.001237	0.001819	0.002414	0.00276	0.000545
Case 7	0.001361	0.001741	0.002488	0.003281	0.003722	0.000642